Precision Measurements Using Semiconductor Light Sources:

Applications in Polarimetry and Spectroscopy

A Thesis Submitted to the Committee on Graduate Studies
in Partial Fulfillment of the Requirements for the Degree of Master of Science
in the Faculty of Arts and Science

TRENT UNIVERSITY
Peterborough, Ontario, Canada

Materials Science M.Sc. Program
October 2011

Abstract

Precision Measurements Using Semiconductor Light Sources: Applications in Polarimetry and Spectroscopy

Matthew J. Romerein

This thesis comprises two parts:

Part I describes a method to improve the accuracy with which the polarization state of light can be characterized by the rotating quarter-wave plate technique. Through detailed analysis, verified by experiment, we determine the positions of the optic axes of the retarder and linear polarizer, and the wave plate retardance, to better than 1° for typical signal-to-noise ratios. Accurate determination of the Stokes parameters can be achieved using this technique to determine the precise retardance at each of the wavelengths of interest.

In *Part II*, a theoretical analysis of the Fabry-Perot interferometer and its application to quantitative absorption spectroscopy is presented. Specifically the effects of broadening due to non-monochromatic light sources and examples of non-ideal etalon surfaces on the visibility of absorption features are investigated. The potential of this type of spectrometer for ethanol detection in a portable breath analysis application is discussed.

Keywords: OPTICS, POLARIMETRY, CALIBRATION, ABSORPTION SPECTROSCOPY, FABRY-PEROT INTERFEROMETER

Acknowledgements

The research grants and scholarships that supported the work in this thesis were provided by NSERC, Research Corporation, Ontario Graduate Scholarship in Science and Technology and by Alcohol Countermeasure Systems through the MITACS Accelerate program.

Much of the material contained in *Part I* of this thesis has been obtained through collaboration with Jeffrey N. Philippson, Robert L. Brooks and Ralph C. Shiell. A significant portion of this material has been published in *Applied Optics*. Although the measurement and analysis techniques were developed jointly, J. Philippson was responsible for the measurements and data analysis for the results that appear in Sections 3.5.1 and 3.5.2 and for producing Figures 3.1, 3.2, 3.3, 3.5 and 3.7. The author is grateful for these contributions and for the generous donation of the polarimeter from R. Brooks.

The author would also like to acknowledge Bryan van der Ende for his input and suggestions pertaining to the material in *Part II*, Keith Donnelly for helpful discussions, Lisa Ugray for invaluable Mathematica tips and Ed Wilson for his expert craftsmanship. The author sincerely thanks his family and friends for their encouragement and support and Ralph Shiell for supervising this research and fostering a stimulating work environment.

Contents

List of Figures

List of Tables

Chapter 1

Introduction

Semiconductor light sources have had a rich history of applications since the advent of the p-n junction [1] owing to their versatility, compact size and high efficiency. Light-emitting diodes (LEDs) have come into widespread use as environmentally friendly sources of incoherent light due to their low power consumption and long operating life, and offer an enormous range of peak wavelengths and bandwidths. In the simplest type of LED the active region is the interface between n- and p-doped layers of a semiconductor material such as GaAs, where n-doped and p-doped refer to extra electrons/holes in the valence/conduction band, respectively. This type of diode, known as a homojunction, produces light via *radiative recombination* – when excess electrons and holes recombine across the active layer and emit photons under forward biasing. Another type, the heterojunction, comprises an active layer of one semiconductor material (e.g., GaAs) sandwiched between n- and p-layers of a larger bandgap material such as AlGaAs. The mobile charges from forward biasing are confined to the active layer by the larger bandgap cladding layers, which increases the probability for recombination. Further, the difference in refractive index between the two

materials confines the emitted light to the active area where subsequent absorption is less likely. These advantages improve the efficiency of the active layer and cleaving and polishing opposite sides of the heterojunction results in a cavity with highly reflective end-facets that support lasing. Other choices of semiconductor materials with different bandgaps and different active layer geometries offer a wide range of lasing wavelengths throughout the visible and infrared spectrum [2]. Due to this phenomenal flexibility and their capacity for extremely cost-effective mass production, laser diodes have been in widespread use in bar-code scanners, DVD players and laser pointers for decades and their range of applications continues to grow to this day.

The purpose of this thesis is to investigate two applications in measurement within optical physics that involve semiconductor light sources in our laboratory. *Part I* involves measuring the polarization state of InGaAsP laser beams and refining a well-known measurement technique to increase the precision of such measurements. *Part II* involves a theoretical investigation of Fabry-Perot elatons illuminated by narrow-band light sources such as LEDs with subsequent application to quantitative absorption spectroscopy. A particular example involving ethanol and water vapour spectra is chosen to illustrate the proposed technique.

Chapter 2

Literature review – Precision polarimetry

The rotating quarter-wave plate method is a well-known technique for characterizing the polarization state of light [3]. In this convenient and widely-used method the intensity of light transmitted through a quarter-wave plate and linear polarizer is recorded at a number of azimuthal angles of the retarder's fast-axis from a fixed reference axis. The measured intensities depend on these angles, which we denote $\{\beta_i\}$, the precise retardance of the wave plate, Δ ($\pi/2$ for an ideal quarter-wave plate), and the angle, γ, of the linear polarizer transmission axis from the same fixed reference axis. Accurate determination of the polarization state of incident light, which is often described by the Stokes parameters, therefore requires precise knowledge of $\{\beta_i\}$, Δ and γ.

Much of the content in this chapter has been published in: M. J. Romerein, J. N. Philippson, R. L. Brooks, and R. C. Shiell, "Calibration method using a single retarder to simultaneously measure polarization and fully characterize a polarimeter over a broad range of wavelengths," *Appl. Opt.* **50**, 5382–5389 (2011), and is reproduced here by permission of the Optical Society.

In practice these values are not always known within the desired level of uncertainty [4]. For the first data point ($i = 1$), the retarder's fast axis is typically intended to be aligned with the reference axis. However, precise azimuthal positioning of the often unlabeled optic axes of the retarder and linear polarizer to within $\sim 1^\circ$ is challenging, leading to an offset, β_0, in all β_i and also causing uncertainty in the value of γ. Further, error in the value of Δ can derive from using a quarter-wave plate at wavelengths away from its design wavelength, $\lambda_{\pi/2}^{\text{nom}}$, or from manufacturing tolerances which are typically $\pm 0.01\lambda_{\pi/2}^{\text{nom}}$ for a zero-order quarter-wave plate [5], or from a slight tilt of the retarder from normal incidence [6]. To give one example of the significance of this, an offset of $+3^\circ$ in the retarder alignment and $+1\%$ in the retardance introduces a 13% error in the Stokes parameter S_1 for horizontally polarized light for which S_1 should take a maximum value.

A reliable approach to calibration is therefore necessary for accurate characterization of polarization using this method. Dlugunovich *et al.* [7] have suggested a method for determining coincidence of the positions of the optic axes and calculating the retardance from the calculated Fourier coefficients. However, determination of coincidence would require a laborious trial-and-error process and once coincidence was achieved, the absolute position of the optic axes relative to the reference axis would still not be precisely known. Furthermore, accurate calculation of the retardance derived from the Fourier coefficients requires that both optic axes be precisely aligned with the horizontal reference axis initially when recording the calibration data, which would be approximate at best when using this method.

The calibration technique developed here expands upon one developed by Brooks (RLB) [8, 9]. This technique employed a two-step calibration process using linearly

polarized incident light. In the first step, using an assumed value for Δ, the angle of the linear polarizer transmission axis from $\hat{x}$, which will henceforth be called 'horizontal', and the offset of the retarder fast axis were determined self-consistently from four sets of measurements corresponding to each of the two optics oriented either forward or reversed by rotating about a vertical axis. Because a reversal of an optic element has no effect if an optic axis is aligned either horizontally or vertically for an ideal wave plate, then provided β_0 and γ are correct, the Stokes parameters calculated for each of the four cases will be consistent. Subsequently, Δ was determined with a second self-consistent technique requiring an additional two sets of measurements with vertically polarized incident light and the transmission axis of the linear polarizer in the polarimeter aligned and then crossed with respect to this polarization. To improve the accuracy of all the determined parameters, β_0, Δ and γ, the entire process could be repeated iteratively to convergence.

The calibration method described in Chapter 3 accomplishes for the first time all this in a single set of measurements and also takes into account the deleterious effect of a misalignment between the assumed-vertical rotation axes of the retarder and polarizer, denoted by ϕ, which can occur due to experimental uncertainties. While developing this calibration method, it was found that a small value of ϕ can introduce errors into the calibration and subsequently into the Stokes parameters if it is not accounted for. To demonstrate the success of the method, a set of highly consistent Stokes parameters and calibration parameters for an incident laser beam using within the polarimeter a set of quarter-wave plates that differ in $\lambda_{\pi/2}^{\mathrm{nom}}$ by as much as 116 nm and for three distinct intentional experimental misalignments, $\{\phi^{\mathrm{nom}}\}$ are presented. Using this calibration method, one quarter-wave plate could therefore

in principle encompass measurements across the whole visible spectrum. Moreover, this calibration method does not require prior knowledge of any of β_0, Δ, γ or ϕ.

Chapter 3

Precision measurement of polarization

Waves are arguably one of the most ubiquitous phenomena in nature. Broadly speaking, they constitute some kind of disturbance that propagates in a medium and can be separated into two categories: *longitudinal* waves, with the direction of the disturbance being parallel to the direction in which the wave propagates and *transverse* waves, with the direction of the disturbance being in the plane perpendicular to the propagation direction. Polarization refers to the orientation of the disturbance or displacement in this plane as the transverse wave propagates.

Light is the term usually given to electromagnetic radiation to which the human eye is sensitive and consists of electromagnetic waves that propagate in a vacuum at the speed of light, c, where $c \equiv 299\,792\,458\,\mathrm{m\,s^{-1}}$. In free space, electromagnetic waves

Much of the content in this chapter has been published in: M. J. Romerein, J. N. Philippson, R. L. Brooks, and R. C. Shiell, "Calibration method using a single retarder to simultaneously measure polarization and fully characterize a polarimeter over a broad range of wavelengths," *Appl. Opt.* **50**, 5382–5389 (2011), and is reproduced here by permission of the Optical Society.

can be represented by transverse plane waves that describe the oscillating electric and magnetic fields of which they are comprised. For a single beam, Maxwell's equations dictate that the magnetic field, often described by its complex vector $\tilde{\mathbf{B}}$, oscillates orthogonal to, and in phase with, the electric field, $\tilde{\mathbf{E}}$, satisfying:

$$\tilde{\mathbf{B}} = \frac{\mathbf{k} \times \tilde{\mathbf{E}}}{\omega}, \tag{3.1}$$

where $\mathbf{k}$ is the wavevector in the direction of propagation and ω is the frequency of oscillation. A beam of light traveling in the $\hat{z}$ direction has electric field components $\tilde{E}_x(t)$ and $\tilde{E}_y(t)$ oscillating sinusoidally in the xy-plane. The relative amplitudes of these oscillations, each denoted by E_{0x} and E_{0y}, and the behaviour of the phase difference between them, δ, characterize the *polarization* of the beam of light.

3.1 Stokes parameters

The polarization state of light cannot be determined as a result of a single intensity measurement. However, using a series of measurements of the light intensity transmitted through a sequence of polarization-changing optics, the polarization state of the incident light can be determined. The four Stokes parameters (S_0, S_1, S_2, S_3), defined in terms of the x and y components of the complex electric field vector, are commonly used to characterize the polarization of fully-, partially- or un-polarized light travelling along the z-direction. Using the convention that x lies in the horizontal plane and $\langle \dots \rangle$ denotes a time average, the Stokes parameters are defined as

follows:

$$S_0 \propto \langle|\tilde{E}_x|^2\rangle + \langle|\tilde{E}_y|^2\rangle = E_{0x}^2 + E_{0y}^2 \tag{3.2}$$

$$S_1 \propto \langle|\tilde{E}_x|^2\rangle - \langle|\tilde{E}_y|^2\rangle = E_{0x}^2 - E_{0y}^2 \tag{3.3}$$

$$S_2 \propto \mathrm{Re}\langle\tilde{E}_x\tilde{E}_y\rangle = 2E_{0x}E_{0y}\cos\delta \tag{3.4}$$

$$S_3 \propto \mathrm{Im}\langle\tilde{E}_x\tilde{E}_y\rangle = 2E_{0x}E_{0y}\sin\delta. \tag{3.5}$$

where S_0 is the intensity of the light, S_1 is the excess of horizontal over vertical linearly-polarized light, S_2 is the excess of $+45^\circ$ over -45° linearly-polarized light, and S_4 is the excess of right over left circularly-polarized light. In general,

$$S_0^2 \geq S_1^2 + S_2^2 + S_3^2, \tag{3.6}$$

where the equality corresponds to fully-polarized light while $S_1^2 + S_2^2 + S_3^2 = 0$ corresponds to un-polarized light. The degree of polarization is expressed by the ratio of the polarized component to the total intensity of the light:

$$P = \frac{\sqrt{S_1^2 + S_2^2 + S_3^2}}{S_0}. \tag{3.7}$$

A Stokes vector, $\mathbf{S}$, normally represented as a column vector, can be constructed from the four Stokes parameters. Typically the Stokes vector is normalized such that $S_0 = 1$, resulting in dimensionless quantities that are independent of the intensity of the light; such an approach is taken throughout this thesis.

3.2 Optical element representation

The polarizing effect of any optical element can be represented by a 4×4 matrix following the formalism developed by Mueller [10]. An ideal linear polarizer (i.e. assuming negligible absorption) with its transmission axis horizontal can be represented by the following matrix:

$$\underline{\underline{\mathbf{M}}}_{\text{pol}} = \frac{1}{2}\begin{bmatrix} 1 & 1 & 0 & 0 \\ 1 & 1 & 0 & 0 \\ 0 & 0 & 0 & 0 \\ 0 & 0 & 0 & 0 \end{bmatrix}. \tag{3.8}$$

The Mueller matrix of an ideal retarder with its fast axis horizontal is given by:

$$\underline{\underline{\mathbf{M}}}_{\text{ret}} = \begin{bmatrix} 1 & 0 & 0 & 0 \\ 0 & 1 & 0 & 0 \\ 0 & 0 & \cos\Delta & \sin\Delta \\ 0 & 0 & -\sin\Delta & \cos\Delta \end{bmatrix}. \tag{3.9}$$

where Δ is the phase shift that it imparts between the components of the electric field lying parallel to its fast and slow axes, respectively.

If the optic axis is rotated to an angle θ from the horizontal axis, the matrix representing that optical element must be rotated by θ using the rotation matrix, $\underline{\underline{\mathbf{R}}}(\theta)$, and its inverse, $\underline{\underline{\mathbf{R}}}^{-1}(\theta)$, as follows [11]:

$$\underline{\underline{\mathbf{M}}}(\theta) = \underline{\underline{\mathbf{R}}}^{-1}(\theta)\,\underline{\underline{\mathbf{M}}}\,\underline{\underline{\mathbf{R}}}(\theta), \tag{3.10}$$

where

$$\underline{\underline{\mathbf{R}}}(\theta) = \begin{bmatrix} 1 & 0 & 0 & 0 \\ 0 & \cos 2\theta & \sin 2\theta & 0 \\ 0 & -\sin 2\theta & \cos 2\theta & 0 \\ 0 & 0 & 0 & 1 \end{bmatrix} \tag{3.11}$$

and

$$\underline{\underline{\mathbf{R}}}^{-1}(\theta) = \begin{bmatrix} 1 & 0 & 0 & 0 \\ 0 & \cos 2\theta & -\sin 2\theta & 0 \\ 0 & \sin 2\theta & \cos 2\theta & 0 \\ 0 & 0 & 0 & 1 \end{bmatrix}. \tag{3.12}$$

The Mueller matrices for an ideal linear polarizer with its transmission axis rotated by γ from horizontal and a retarder with its fast axis rotated by β from horizontal obtained using Eqs. (3.8) and (3.9) respectively in Eq. (3.10) are:

$$\underline{\underline{\mathbf{M}}}_{\text{pol}}(\gamma) = \frac{1}{2}\begin{bmatrix} 1 & \cos 2\gamma & \sin 2\gamma & 0 \\ \cos 2\gamma & \cos^2 2\gamma & \frac{1}{2}\sin 4\gamma & 0 \\ \sin 2\gamma & \frac{1}{2}\sin 4\gamma & \sin^2 2\gamma & 0 \\ 0 & 0 & 0 & 0 \end{bmatrix}, \tag{3.13}$$

$$\underline{\underline{\mathbf{M}}}_{\text{ret}}(\beta) = \begin{bmatrix} 1 & 0 & 0 & 0 \\ 0 & \cos^2 2\beta + \sin^2 2\beta \cos\Delta & \frac{1}{2}\sin 4\beta(1-\cos\Delta) & -\sin 2\beta \sin\Delta \\ 0 & \frac{1}{2}\sin 4\beta(1-\cos\Delta) & \sin^2 2\beta + \cos^2 2\beta \cos\Delta & \cos 2\beta \sin\Delta \\ 0 & \sin 2\beta \sin\Delta & -\cos 2\beta \sin\Delta & \cos\Delta \end{bmatrix}. \tag{3.14}$$

The polarization state emerging from any sequence of optics can be determined by calculating the product of their matrices and the incident Stokes vector. For example, the Stokes vector, $\mathbf{S}'$, for light transmitted first through a retarder with its fast axis rotated to β from horizontal and then a linear polarizer with its transmission axis rotated to γ from horizontal can be calculated as follows:

$$\mathbf{S}' = \underline{\underline{\mathbf{M}}}_{\text{pol}}(\gamma)\,\underline{\underline{\mathbf{M}}}_{\text{ret}}(\beta)\mathbf{S}. \tag{3.15}$$

3.3 Theory of the rotating quarter-wave plate method

The classical method for measuring polarization employs a quarter-wave plate ($\Delta = \pi/2$) with its fast axis fixed in space and aligned with the x-axis and a subsequent linear polarizer rotated to different angles, γ, from the x-axis as defined by the optical elements comprising the polarimeter. Three measurements would be taken with the retarder removed and the polarizer set to $\gamma = \{0°, 45°, 90°\}$, and the final measurement with the retarder in place and $\gamma = 45°$. This method, while satisfactory, is problematic for several reasons: it relies upon accurate positioning of the polarizer's transmission axis; it uses only four measurements, increasing the chance for random errors; and the introduction of the retarder for the last measurement results in the absorption of some light, changing the intensity incident on the polarizer and thus introducing a systematic error [12].

The rotating quarter-wave plate method is an alternative approach in which the transmitted intensity is measured with the polarizer's angle kept fixed while the retarder's fast axis is rotated to a set of angles, $\{\beta_i\}$, from the x-axis. This method has the advantage that an increased number of retarder angles can be used to reduce

random errors and it remains in the beam path for the entire set of measurements, eliminating systematic error in the total intensity. The relevant angles of optical elements in the rotating quarter-wave plate polarimeter are shown in Fig. 3.1(a).

with the values of Δ and γ absorbed within the Fourier coefficients:

$$I(\beta_i) = \frac{1}{2}(a_0 + a_2 \cos 2\beta_i + b_2 \sin 2\beta_i + a_4 \cos 4\beta_i + b_4 \sin 4\beta_i). \tag{3.17}$$

The minimum number of intensity measurements required in order to determine a_0, a_2, b_2, a_4 and b_4 is 5. For a set of N intensity measurements taken at equally spaced values of β_i ranging from 0 to $(N-1)\pi/N$ (effectively spanning 0 to π), the Fourier coefficients can be found from:

$$a_0 = \frac{2}{N} \sum_{i=1}^{N} I_i \tag{3.18}$$

$$a_2 = \frac{4}{N} \sum_{i=1}^{N} I_i \cos 2\beta_i \tag{3.19}$$

$$b_2 = \frac{4}{N} \sum_{i=1}^{N} I_i \sin 2\beta_i \tag{3.20}$$

$$a_4 = \frac{4}{N} \sum_{i=1}^{N} I_i \cos 4\beta_i \tag{3.21}$$

$$b_4 = \frac{4}{N} \sum_{i=1}^{N} I_i \sin 4\beta_i. \tag{3.22}$$

Using additional measurements with the same spacing of β_i between π and 2π still allows Eqs. (3.18)–(3.22) to be used but also compensates for systematic errors due to possible inhomogeneities in the retarder.

Provided that $\{\beta_i\}$, Δ, and γ are accurately known, the Stokes vector of the

incident light can then be derived using the intensity data as follows:

$$S_0 = a_0 - \frac{1+\cos\Delta}{1-\cos\Delta}(a_4\cos 4\gamma + b_4 \sin 4\gamma) \tag{3.23}$$

$$S_1 = \frac{2}{1-\cos\Delta}(a_4\cos 2\gamma + b_4 \sin 2\gamma) \tag{3.24}$$

$$S_2 = \frac{2}{1-\cos\Delta}(b_4\cos 2\gamma - a_4 \sin 2\gamma) \tag{3.25}$$

$$S_3 = \frac{a_2}{\sin\Delta\sin 2\gamma} = -\frac{b_2}{\sin\Delta\cos 2\gamma}. \tag{3.26}$$

In the case where $\beta_0 \neq 0$ (there is a finite but unknown offset between the retarder fast axis and $\hat{x}$), an accurate calibration requires replacing β_i with $\beta_i + \beta_0$ in Eqs. (3.18)–(3.22) to correct for this. However, using the sum-difference trigonometric formulae, β_0 can be factored out of the Fourier coefficients and absorbed into Eqs. (3.23)–(3.26). Reversing each optic by rotating about a vertical axis is equivalent to reflecting the optic axes in the horizontal reference axis, so β_0 and γ become $-\beta_0$ and $-\gamma$. The axis orthogonal to the vertical rotation axis of the *polarizer* was chosen to be the horizontal reference axis. The offset of the retarder fast axis must then also be measured from the horizontal axis. If its front-to-back rotation axis is offset from the polarizer's vertical rotation axis by ϕ in the plane of the retarder's azimuthal rotation, $-\beta_0$ must instead be replaced with $-(\beta_0 - 2\phi)$ when the retarder is reversed as depicted in Fig. 3.1(b). The normalized Stokes vectors calculated for the four possible cases with each optic oriented either forward or reversed could be expected to be inconsistent unless the values for β_0, Δ, γ and ϕ are correct.

The formulae for calculating the Stokes vector when both optics are forward

(case 1) and only the linear polarizer is reversed (case 3):

$$S_0^{(1,3)} = a_0 - \frac{(1+\cos\Delta)}{(1-\cos\Delta)}[a_4\cos 4(\gamma \mp \beta_0) \pm b_4 \sin 4(\gamma \mp \beta_0)] \tag{3.27}$$

$$S_1^{(1,3)} = \frac{2}{(1-\cos\Delta)}[a_4\cos 2(\gamma \mp 2\beta_0) \pm b_4 \sin 2(\gamma \mp 2\beta_0)] \tag{3.28}$$

$$S_2^{(1,3)} = \frac{2}{(1-\cos\Delta)}[b_4\cos 2(\gamma \mp 2\beta_0) \mp a_4 \sin 2(\gamma \mp 2\beta_0)] \tag{3.29}$$

$$S_3^{(1,3)} = \pm\frac{a_2}{\sin\Delta\sin 2(\gamma \mp \beta_0)} = -\frac{b_2}{\sin\Delta\cos 2(\gamma \mp \beta_0)}, \tag{3.30}$$

where the upper sign corresponds to case 1 and the lower sign corresponds to case 3, and when only the retarder is reversed (case 2) and when both optics are reversed (case 4):

$$S_0^{(2,4)} = a_0 - \frac{(1+\cos\Delta)}{(1-\cos\Delta)}[a_4\cos 4(\gamma \pm \beta_0 \mp 2\phi) \pm b_4 \sin 4(\gamma \pm \beta_0 \mp 2\phi)] \tag{3.31}$$

$$S_1^{(2,4)} = \frac{2}{(1-\cos\Delta)}[a_4\cos 2(\gamma \pm 2\beta_0 \mp 4\phi) \pm b_4 \sin 2(\gamma \pm 2\beta_0 \mp 4\phi)] \tag{3.32}$$

$$S_2^{(2,4)} = \frac{2}{(1-\cos\Delta)}[b_4\cos 2(\gamma \pm 2\beta_0 \mp 4\phi) \mp a_4 \sin 2(\gamma \pm 2\beta_0 \mp 4\phi)] \tag{3.33}$$

$$S_3^{(2,4)} = \pm\frac{a_2}{\sin\Delta\sin 2(\gamma \pm \beta_0 \mp 2\phi)} = -\frac{b_2}{\sin\Delta\cos 2(\gamma \pm \beta_0 \mp 2\phi)}, \tag{3.34}$$

where the upper sign corresponds to case 2 the lower sign to case 4. Here, for each of the four cases the Fourier coefficients a_0–b_4 require calculation only once for any number of values of β_0 considered since it is absorbed into Eqs. (3.27)–(3.34). If the correct values of β_0, Δ, γ and ϕ are used, the normalized Stokes vectors calculated for each of the four cases are expected to be consistent. An additional linear polarizer (LP$'$) set to provide incident light with comparable S_1 and S_2 components (i.e. set approximately to $\pm 22.5°$ or $\pm 67.5°$) ensures that consistency can be determined

for values of S_1/S_0 and S_2/S_0 well above the experimental uncertainty. However, we found that coupling between β_0, Δ and ϕ leads to multiple possible values of these parameters that produce, within experimental uncertainty, equally consistent results for the calculated Stokes vectors but with incorrect values for the degree of polarization. Fully polarized incident light (due to LP$'$) adds the requirement that $P^{(j)} = 1$ for all j as recognized and used also in [13]. Therefore, to determine the set of parameters $\{\beta_0, \Delta, \gamma, \phi\}$ closest to the correct values, calculation of the variances of $S_1^{(j)}/S_0^{(j)}$ and $S_2^{(j)}/S_0^{(j)}$ added to the sum of the squared differences between $P^{(j)}$ and 1 for each j, forms a quantity dependent upon both the scatter of S_1 and S_2 and the radial distances of the end points of $\mathbf{S}^{(j)}$, anchored at the origin, from the surface of the unit Poincaré sphere [14]:

$$\xi = \sum_{j=1}^{4} \left[\left(\frac{S_1^{(j)}}{S_0^{(j)}} - \left\langle \frac{S_1}{S_0} \right\rangle \right)^2 + \left(\frac{S_2^{(j)}}{S_0^{(j)}} - \left\langle \frac{S_2}{S_0} \right\rangle \right)^2 + (1 - P^{(j)})^2 \right]. \tag{3.35}$$

Here the summation is over the 4 cases and $\langle \ldots \rangle$ denotes the arithmetic mean. The value of ξ takes a minimum at the position in $\{\beta_0, \Delta, \gamma, \phi\}$ space given by the correct values of these parameters. Note that we have hitherto assumed β_0 refers to the angle of the retarder's *fast* axis from the reference axis. Since S_3 is squared in Eq. (3.7), this calibration method does not distinguish its fast and slow axes so one additional measurement is required using a circular polarizer to resolve this ambiguity if required. For example, if a circular polarizer placed before the polarimeter is used to produce right circularly-polarized incident light and β_0 is set approximately to 45°, then the resultant light will be predominantly vertically linearly-polarized (depending on how close Δ is to $\pi/2$) if β_0 corresponds with the fast axis. Conversely, the resultant

light will be predominantly horizontally linearly-polarized if β_0 corresponds with the slow axis. This can be determined using a polarizing beam-splitter placed after the polarimeter with the linear polarizer in the polarimeter removed.

In summary, calibration of the polarimeter involves using linearly polarized incident light and calculating the Fourier coefficients for each of the four cases using Eqs. (3.18)–(3.22) and subsequently mapping out $\xi(\beta_0, \Delta, \gamma, \phi)$ where $S_0 - S_3$ are obtained from Eqs. (3.27)–(3.34). The polarization state of any light with unknown polarization can then be precisely found by removing the additional linear polarizer, measuring a set of intensities $\{I_i\}$, and calculating the Stokes vector for this light using Eqs. (3.27)–(3.30) and the parameter values corresponding to the minimum previously found in ξ as illustrated in section 3.5.1.

3.4 Experimental setup

The original motivation for precisely measuring the polarization state of light and subsequently refining the rotating quarter-wave plate technique was to characterize the polarization of InGaAsP laser diodes in an external cavity configuration. Given this, a Philips CQL806 high-power laser diode was used for all measurements. The optical train for the polarimeter calibration and polarization measurement experiment involved light from the laser diode being coupled into a single-mode optical fiber to improve its spatial intensity profile (see Section 3.4.1 for further details). The fiber coupler was preceded by a Faraday rotator-type optical isolator (OI) to prevent back-reflections from destabilizing the laser. Upon exiting the fiber, the near-TEM_{00} beam was expanded to $\sim 8\,\text{mm}$ in diameter with a pair of plano-convex lenses. A highly horizontally linearly polarized beam was then produced by two consecutive polarizing

beam-splitters (PBSs). The s-polarized reflection from the first was sent to an optical spectrum analyzer (OSA) to monitor the mode structure of the laser in real-time. The very weak reflection from the second was sent to a reference photodiode for power normalization in the event of laser drift. The p-polarized beam exiting the second PBS was to be analyzed by the polarimeter which was preceded by the additional linear polarizer (LP′) during the calibration procedure. Polarization insensitive neutral density filters (NDs) were used to attenuate the beam exiting the polarimeter in order to take advantage of the full analog-to-digital conversion range of the microcontroller that processed the measured signals. This beam and the reference beam were focused onto OPT101 photodiodes for the calibration and subsequent intensity measurements. The experimental setup is illustrated in Fig. 3.2. Details of each component of the experimental setup are given below:

3.4.1 Fiber coupling

A popular technique for improving the spatial intensity profile of a laser beam is to couple it into a single-mode fiber. Due to the extremely small diameter of the fiber core ($\sim 5\,\mu$m), only the lowest order transverse mode (TEM_{00}) can propagate within it. This means that the output beam from the fiber collimator is TEM_{00} with a Gaussian intensity profile. This profile was desirable for measuring the polarization of the beam in order to sample the entire retarder face (after beam expansion with two plano-convex lenses) with an azimuthally uniform intensity profile in order to average out any small spatial inhomogeneities in the material's birefringence.

To develop our approach, a helium-neon laser ($\lambda = 633$ nm) was initially coupled

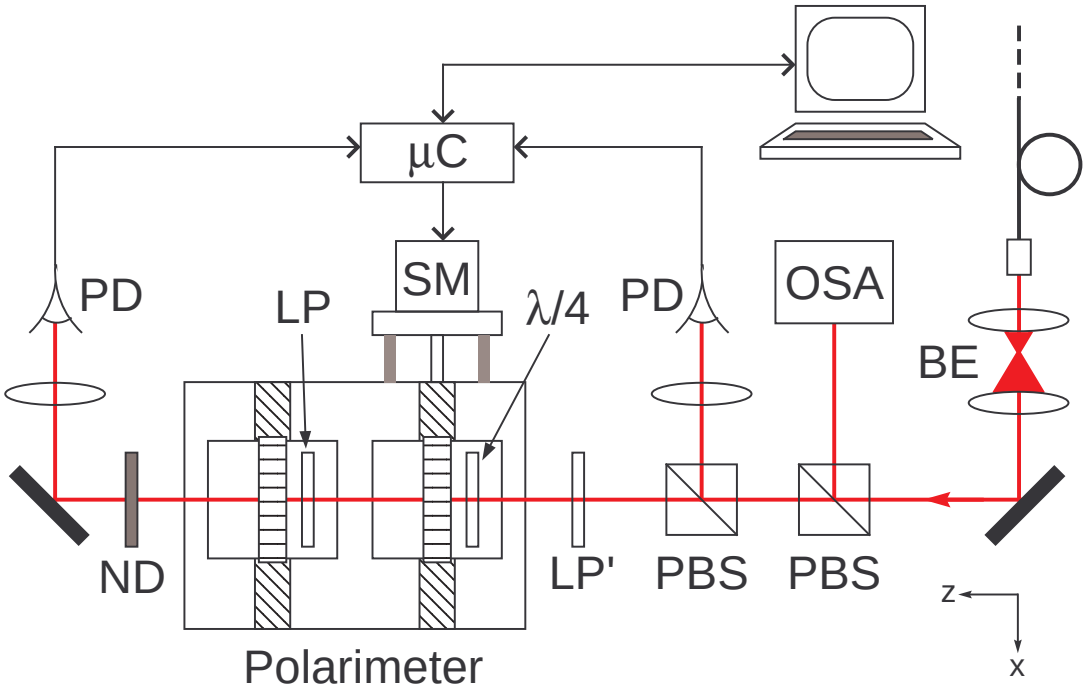

Figure 3.2: Schematic of the experimental setup. The beam under test originates from an external-cavity diode laser after which its diameter is increased to $\sim 8\,\mathrm{mm}$ by a beam expander (BE). A pair of polarizing beam-splitters (PBS) produce a horizontally-polarized beam with which to test the calibration method. The first s-polarized reflection is sent to an optical spectrum analyzer (OSA), while the weak second reflection serves as a reference for power normalization. The polarimeter itself consists of a quarter-wave plate ($\lambda/4$) and linear polarizer (LP) in rotational mounts. The calibration method employs an additional linear polarizer (LP$'$) set to make $S_1 \approx S_2$ and is removed for regular beam analysis. The retarder is rotated via a worm gear by the stepper motor (SM) and the transmitted light is measured by a photodiode (PD) after attentuation by a neutral density filter (ND). The microcontroller (μC) controls both the SM and records the PD voltages for transmission to a computer.

into a single-mode optical fiber with 65% efficiency. Optimal coupling requires Gaussian mode-matching of the fiber and the beam. This means that the beam should have a near Gaussian intensity profile and the $1/e^2$ beam width should match the

mode field diameter, MFD, of the fiber core. The He-Ne laser was chosen to investigate fiber-coupling since it is known to have an approximately Gaussian beam profile. The Gaussian wavefronts should be planar when they meet the fiber tip for optimal coupling into the core. This means that an appropriate lens should be used that will focus the beam down to the MFD at the beam waist (the narrowest width, corresponding to the focal point in a ray optics picture) and this beam waist should be positioned at the fiber tip. An A375TM-B 7.5 mm focal length aspheric lens from Thorlabs (with an RMS wavefront error of 0.028 waves and 40-20 Scratch-Dig surface quality) was suggested for this application by a colleague*. The type of single-mode fiber suitable for these wavelengths (SM600) has a MFD of 4.3 μm @ 633 nm and 4.6 μm @ 680 nm.

Gaussian beam analysis

The *spot size* (the distance from the beam axis to where the intensity drops to $1/e^2$ of its maximum value, i.e. half of the $1/e^2$ width) of a perfect Gaussian beam as it propagates is described by [15]:

$$w^2(z) = w_0^2 \left(1 + \frac{z^2}{z_R^2}\right), \tag{3.36}$$

where w_0 is the smallest spot size, called the beam waist (assumed to be positioned at $z = 0$) and z_R is the Rayleigh range (the distance from the waist at which the spot size reaches $\sqrt{2}\, w_0$). The Rayleigh range is given by:

$$z_R = \frac{\pi w_0^2}{\lambda}, \tag{3.37}$$

*The author would like to acknowledge Fredrik Fatemi for this suggestion

where λ is the wavelength of the light. The appropriate spot size incident on the 7.5 mm lens for mode-matching with SM600 fiber can be derived using Eq. (3.36) and simple trigonometry. In the far field (far beyond the Rayleigh range) the spot size is approximately:

$$w(z >> z_R) \approx \frac{z\lambda}{\pi w_0}. \tag{3.38}$$

From this approximation we can derive the divergence angle, θ, of the beam in terms of the spot size of the beam waist and the wavelength of light:

$$\tan\theta \approx \frac{\lambda}{\pi w_0}. \tag{3.39}$$

For optimal coupling into the fiber core, we want the width of the beam (twice the spot size) at its waist to be equal to the MFD of the fiber:

$$w_0 = \frac{\text{MFD}}{2}. \tag{3.40}$$

If we assume that the beam incident on the coupling lens is collimated, then the beam waist will be located at a distance equal to the focal length of the lens, f, from its principle plane. Following from this, the divergence angle can also be expressed in terms of the focal length of the lens and the spot size of the collimated beam, w_c:

$$\tan\theta = \frac{w_c}{f}. \tag{3.41}$$

By equating Eqs. (3.39) and (3.41), the spot size of the collimated beam can be related to the MFD, f, and λ. Since these parameters are already specified, all that is required for optimal coupling is a highly collimated beam of the appropriate spot

size given by:

$$w_c \approx \frac{2\lambda f}{\pi \mathrm{MFD}}. \tag{3.42}$$

A rigorous approach to fulfilling these requirements for a given beam involves determining the complex radius of curvature, $\tilde{q}(z)$, which describes how the beam's wavefronts evolve as it propagates, through fitting Eq. (3.36) to a series of spot size measurements obtained with a beam profiler. An ABCD system matrix representing an arbitrary sequence of lenses and distances that satisfy the coupling requirements can subsequently be derived. The results of such an approach enabled coupling of the He-Ne beam into a single-mode fiber with 65% efficiency. This served as a benchmark with which to compare the coupling efficiencies of diode laser beams with non-rotationally symmetric spatial intensity profiles.

Fiber coupling alignment guide

The light from a Lumex SSL-LX100T123SIC high-power red LED (with peak wavelength at 636 nm) coupled into the 'free' end of the fiber was found to produce an adequate guide beam in a darkened room for aligning the fiber-coupling apparatus with the He-Ne cavity prior to switching it on. A schematic of a simple alignment device that was designed and built for this purpose is shown in Fig. 3.3. A cone of polished aluminum with 0.5 mm threading to accept that of the output end of a Thorlabs FC260APC-B fiber collimation package was fabricated to efficiently couple light from the LED into the intended output end of the fiber. The guide beam exiting the through the coupling lens was then overlapped with the beam to be coupled using two mirrors.

Upon removing this alignment guide from the output collimator, coupled laser

light could already be seen at the output. Fine tuning of the z position of the coupling lens and re-adjustment of the x and y tilt of the fiber coupler and alignment mirrors was subsequently required. The use of this alignment guide drastically reduced the time required to achieve a satisfactory coupling efficiency ($\sim 45\%$) when coupling laser diode beams into a single-mode fiber.

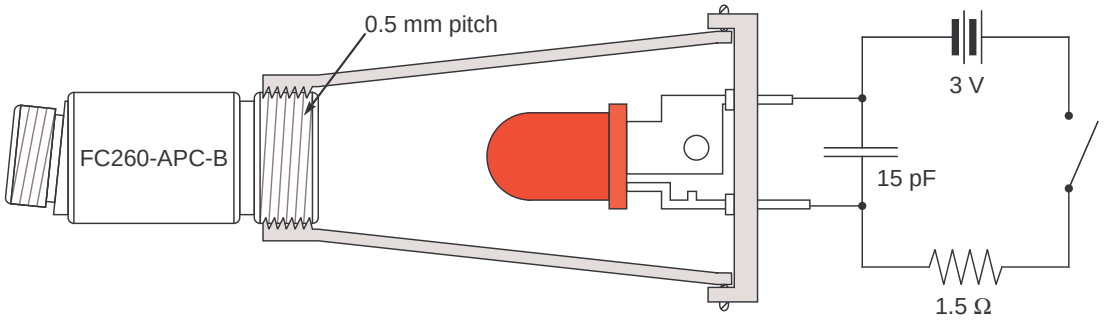

Figure 3.3: Fiber coupling alignment guide.

3.4.2 Polarimeter

The polarimeter consists of a retarder and linear polarizer placed in removeable rotational mounts [9]. Light passes first through the retarder and then the linear polarizer and the transmitted intensity is measured with a detector as shown in Fig. 3.2. An initially undetermined (fast or slow) optic axis of the retarder is initially set approximately parallel to the horizontal reference axis, $\hat{x}$, by retroreflecting a horizontally polarized beam through the retarder and minimizing the vertically polarized component using a PBS. The linear polarizer transmission axis is kept at a fixed angle γ from $+\hat{x}$. It was found that the calibration procedure was most robust with γ fixed near $\pm 45°$ which is straight-forward to determine with a PBS temporarily placed after the linear polarizer. The mounts of the retarder and linear polarizer permit front-to-back

(180°) rotation about an axis perpendicular to the direction of beam propagation ($+\hat{z}$) allowing each optic to be oriented either "forward" or "reversed" for the four possible cases used in this calibration method. With the retarder removed, the front-to-back rotation axis of the linear polarizer is set to be vertical by placing a PBS before it and measuring equal transmitted intensities for both forward and reversed orientations. The retarder's front-to-back rotation axis is then set approximately parallel to that of the linear polarizer's by eye ($\phi \approx 0°$).

A series of intensity measurements were taken with LP′ in place and the retarder rotated counter-clockwise (as seen looking toward the light source along $-\hat{z}$) by $N = 50$ equal intervals in 360°. The transmission axis of LP′ was set to provide incident light with comparable S_1 and S_2 components. The retarder's rotational mount was driven by a worm gear where one full rotation of the worm gear advanced the rotational mount by 3.6°. A stepper motor advanced the worm gear by 1.8° per step, offering a precision of 0.01° in the N angles $\{\beta_i + \beta_0\}$ between the horizontal reference axis and the fast axis of the retarder. The stepper motor was controlled by a pair of UC3770AN stepper motor controllers and a PIC18LF2320 microcontroller [18]. The ADC (analog-to-digital) capability of the PIC read and stored voltages from the PDs that monitored the light transmitted through the polarimeter and the reference beam as 10–bit values at each β_i and transmitted them via RS-232 to a computer. Neutral density filters attenuated the transmitted beam in order to achieve maximum resolution within the PIC's 0-5 V ADC range. The transmitted intensities were normalized to the reference intensities to correct for systematic errors caused by laser drift. For each of the four cases, a set of normalized intensity data was obtained and the Fourier coefficients were calculated from Eqs. (3.18)–(3.22). Using Eqs. (3.27)–(3.34), Stokes

vectors were calculated for each case followed by a calculation of ξ using Eq. (3.35) at a range of $\{\beta_0, \Delta, \gamma, \phi\}$ values.

3.4.3 Automation control and data acquisition

Automation of the rotating quarter-wave plate polarimeter was controlled by a Microchip PIC18LF2320 microcontroller. The PIC was programmed to set pins 11 and 21 to output alternating high-low logic signals to the phase inputs of the Unitrode UC3770A stepper motor drivers. A complete high-low sequence sent to both drivers advances the stepper motor by 1.8°. After 400 steps the PIC pauses to receive analog voltage signals on pins 2 and 3 from the photodiodes and stores them as 10–bit values following conversion by its on-board ADC. 50 values are stored in the PIC's memory for transmission at the end of data collection. PC interface via RS-232 was made through output pins 17 and 18 using a Maxim MAX232 driver/receiver.

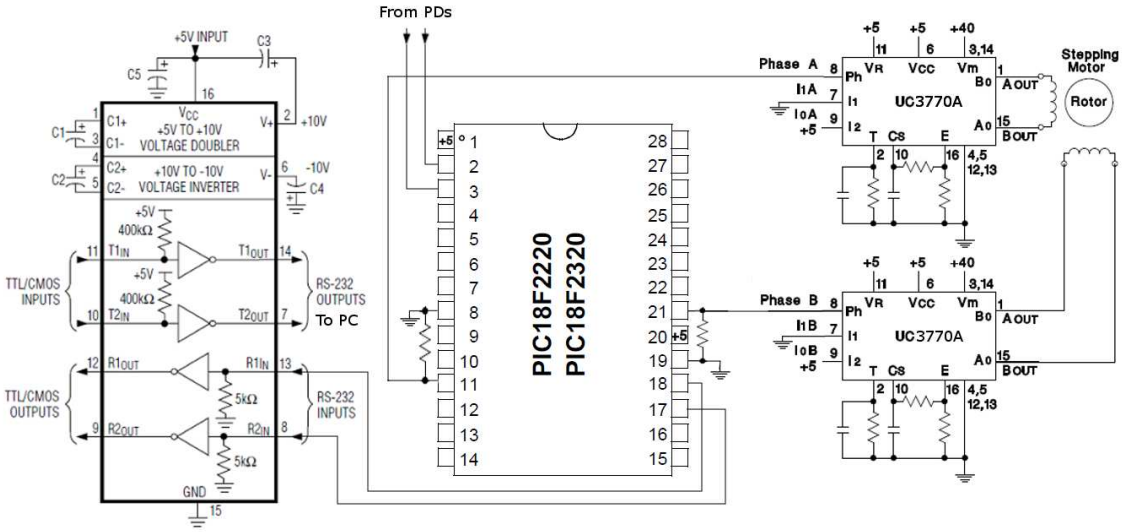

Figure 3.4: The PIC18LF2320 microcontroller controls UC3770A stepper motor drivers and converts analog photodiode voltages to digital signals for output to a PC via RS-232 using a MAX232 driver/receiver

3.5 Results

The calibration scheme involves an iterative 4-dimensional parameter search to find the set of values $\{\beta_0, \Delta, \gamma, \phi\}$ that minimizes ξ. An important consideration is the choice of a suitable sampling resolution in each parameter to obtain the true minimum in a reasonable computational time. We found that an initial sampling resolution of no larger than $\sim 1^\circ$ was necessary to locate the region of the global minimum in parameter space in the first iteration. Typical parameter ranges used for the initial search were:

$$-5^\circ \leq \quad \beta_0 \quad \leq 5^\circ \tag{3.43}$$

$$\left(\frac{\lambda_{\pi/2}^{\text{nom}}}{\lambda}\right) 85^\circ \leq \quad \Delta \quad \leq \left(\frac{\lambda_{\pi/2}^{\text{nom}}}{\lambda}\right) 95^\circ \tag{3.44}$$

$$40^\circ \leq \quad \gamma \quad \leq 50^\circ \tag{3.45}$$

$$-5^\circ \leq \quad \phi \quad \leq 5^\circ, \tag{3.46}$$

The range of Δ is sufficient to find the retardance of a quarter-wave plate within manufacturing tolerances if an approximate value has been assumed from the design wavelength. The ranges of β_0, γ and ϕ allow for typical experimental uncertainties in the alignment of the optics in the polarimeter described above. Experimental results of nine calibrations using this search are presented in Section 3.5.2.

3.5.1 Simulation of the calibration method

The validity of the calibration method was analyzed by choosing specific values for β_0, Δ, γ and ϕ and generating simulated intensity data with a typical signal-to-noise ratio (SNR) of 40 for each of the four cases. For each case and each value of $(\beta_0, \Delta, \gamma, \phi)$,

ξ was mapped with an initial sampling resolution of $\sim 1^\circ$ in all parameters. In successive iterations, the sampling interval of each parameter was halved while keeping the number of samples fixed and the new range was centered at the position of the minimum value of ξ from the previous iteration. Using simulated data with random noise added for an incident Stokes vector corresponding to light polarized at 67.5°, $\beta_0 = 2^\circ$, $\Delta = 0.26 \times 2\pi = 93.6^\circ$, $\gamma = 44^\circ$, $\phi = 1^\circ$, the following values were found after 10 search iterations: $\beta_0^{\text{calc}} = 1.91^\circ$, $\Delta^{\text{calc}} = 93.56^\circ$, $\gamma^{\text{calc}} = 43.93^\circ$, $\phi^{\text{calc}} = 0.92^\circ$. For illustration, a cut through the surface of $\log_{10}[\xi(\beta_0, \Delta)]$ showing its dependence on β_0 and Δ is graphically depicted in Fig. 3.5. As expected this shows a global minimum very close to the position of the correct values.

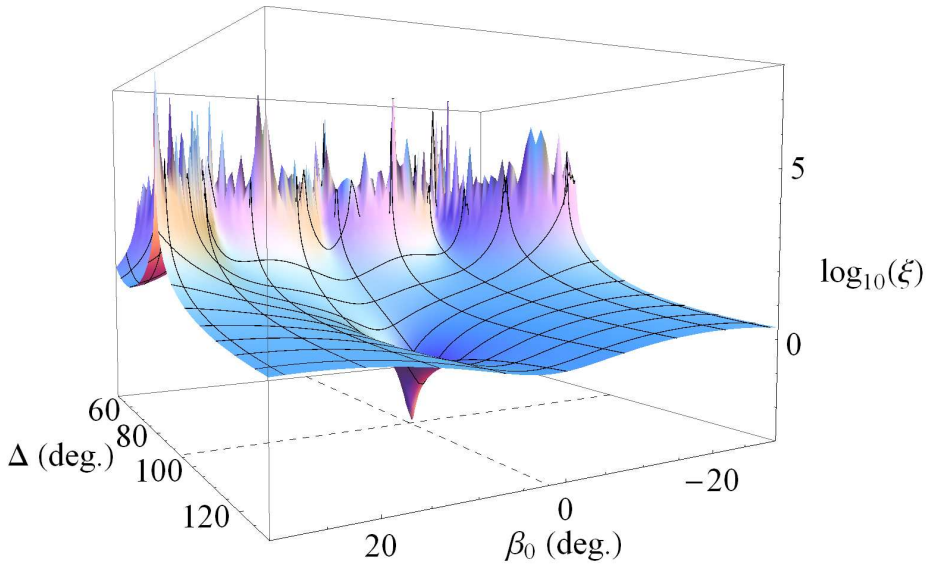

Figure 3.5: The dependence of ξ on β_0 and Δ using the values $\gamma = 43.93^\circ$ and $\phi = 0.9221$

dependence of ξ on β_0 and Δ for the same simulated data, one in red assuming $\phi = 0°$ (i.e. not including ϕ in the parameter search), and another in blue using the value obtained for ϕ from the search. The position of the erroneous minimum is indicated with dashed lines while the true values of β_0 and ϕ are indicated with solid lines.

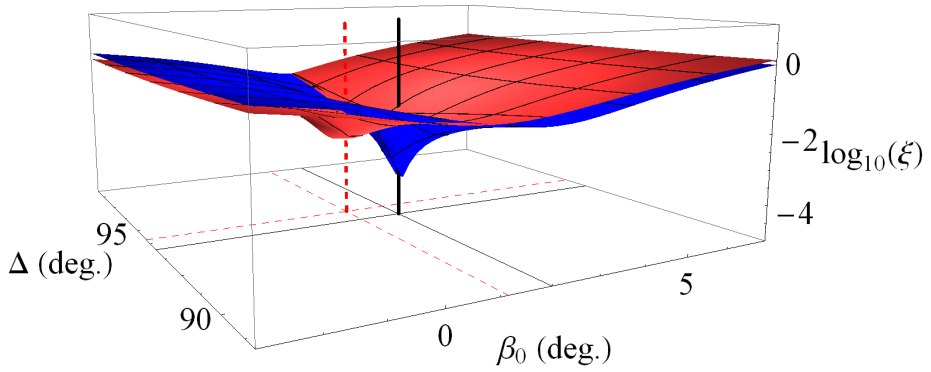

Figure 3.6: The dependence of ξ on β_0 and Δ for data generated using $\phi = 1°$ with noise added. The two surfaces were plotted assuming values of $\phi = 0°$ (minimum indicated by dashed lines, red) and $\phi = 0.92°$ (minimum located close to the intersection of the solid lines, blue) with a 5 mrad sampling resolution. The solid lines indicate the chosen values of β_0 and Δ while the dashed lines indicate the erroneous minimum.

The robustness of the calibration scheme and an indication of its applicability in practice was determined by adding different levels of random noise to the simulated data and calculating the absolute differences between the correct parameter values and those found after eight iterations, averaged over 20 calibration simulations, for 41 values of SNR (see Fig. 3.7). The data was simulated using the same parameter values as were used for Figs. 3.5 and 3.6. This indicates that a SNR greater than 7 is sufficient to obtain all parameters to within $\sim 1°$ of the correct values using this calibration method.

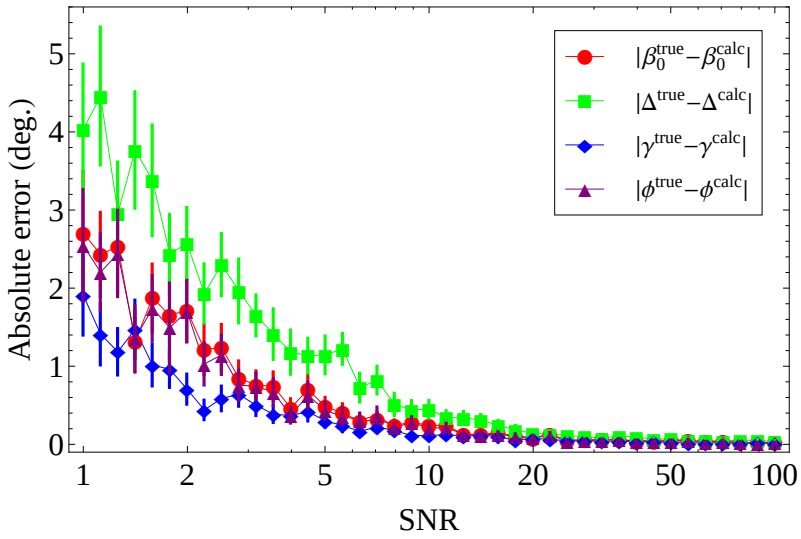

Figure 3.7: Analysis of calibration results for simulated data with added random noise using parameter values: $\{\beta_0, \Delta, \gamma, \phi\} = \{2°, 0.26 \times 2\pi = 93.6°, 44°, 1°\}$. Each datum is the average over 20 sets of results with the same SNR value. For comparison, data used to construct Table 3.1 had SNR values in the range 40–61 for the three different retarders.

3.5.2 Experimental verification of the calibration method

The broad applicability of this calibration method was demonstrated using three different quarter-wave retarders with 672.7 nm light from a fiber-coupled laser diode. A beam-expander increased the beam-width to ~ 8 mm to average over inhomogeneities in the polarimeter optics. True zero-order mica wave plates were used with design wavelengths $\lambda_{\pi/2}^{nom} = \{670\text{ nm}, 645\text{ nm}, 548\text{ nm}\}$. These design wavelengths correspond to retardances of 89.6°, 86.4° and 74.4° respectively at the optical wavelength used [19], taking account of the variation of birefringence with wavelength in mica [20]. Note that inconsistencies in the published data for the dispersion of mica birefringence make these values necessarily approximate [21]. Additionally, to demonstrate the reliability of this calibration technique against experimental misalignment, for each retarder the polarimeter was calibrated for three different values of ϕ by

intentionally misaligning the retarder's front-to-back rotation axis in the plane of its azimuthal rotation by $\phi^{\text{nom}} = \{-3.6°, 0, +3.6°\}$ (see Fig. 3.8). The fast axis of each retarder was approximately aligned with $\hat{x}$ ($\beta_0 \approx 0$). For each of the nine calibrations, the linear polarizer transmission axis was kept at a fixed angle γ from $\hat{x}$. The results of these nine calibrations are presented in Table 3.1. We expect consistency between the three values determined for β_0 and Δ for each retarder and further, the results for γ and $\phi - \phi^{\text{nom}}$ should be consistent between all nine calibrations. The observations follow these predictions with the expected similarities clearly visible within each column, and for γ and $\phi - \phi^{\text{nom}}$ throughout the whole table. Further, analysis of the 670 nm wave plate using 777.6 nm light resulted in values $\beta_0 = 4.46°$, $\gamma = 144.15°$ and $\phi - \phi^{\text{nom}} = 1.88°$, all within $\sim 1°$ of the values obtained at 672.7 nm, and $\Delta = 76.76°$, within $\sim 1°$ of the nominally expected value of $670/780 \times 90°$. These small variations may be attributed to the realignment required to change to a light-source at a different wavelength. Due to the fixed separation between the lens and the fiber tip within the fiber collimator, the 777.6 nm beam emerged with a slightly different divergence angle. This required realignment of the beam-expanding lenses to obtain a well-collimated beam after expansion. This realignment may have changed the beam's angle of incidence with the polarimeter optics, thus changing the reference frame from which the angles of the optics' axes were measured.

To verify that each of the nine calibrations could individually provide a normalized Stokes vector consistent with the incident polarization state, LP′ was removed and an additional set of intensity data was recorded with horizontally-polarized incident light provided by the two consecutive polarizing beam-splitters. These results are presented in Table 3.2. We expect consistency between the calculated Stokes vectors,

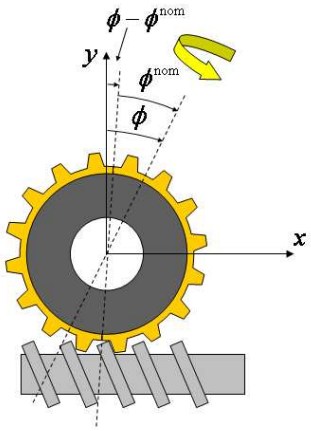

Figure 3.8: Illustration of the intentional offset of the retarder's front-to-back rotation axis from approximately vertical, ϕ^{nom}, the value of its actual offset from the y-axis, ϕ, as determined by the calibration method and the difference between these two values, $\phi - \phi^{\text{nom}}$, which is expected to be constant for any value of ϕ^{nom}.

and for these to correspond to that for horizontally polarized light. The nine Stokes vectors are indeed highly consistent with one another, as shown by the low standard errors in S_1, S_2 and S_3 in Eq. (3.47). The mean values of the normalized Stokes parameters and the degree of polarization with the standard errors derived from these measurements are:

$$\langle \mathbf{S} \rangle = \begin{pmatrix} 1.000 \\ 0.995 \pm 0.001 \\ 0.121 \pm 0.002 \\ 0.0158 \pm 0.0003 \end{pmatrix} \tag{3.47}$$

$$\langle P \rangle = 1.002 \pm 0.001. \tag{3.48}$$

The average value for S_3 indicates a consistent small ellipticity angle[†] ($\chi = 0.5°$), possibly due to stress-induced birefringence in a polarizing beam-splitter. The values for S_1 and S_2 reflect a small ($\sim 3°$) misalignment between the transmission axis of the second polarizing beam-splitter and the horizontal reference axis defined to be perpendicular to the linear polarizer's front-to-back rotation axis. While the expected value of unity for P does not lie within the standard error of its mean value, this value is acceptably close to unity and the slight deviation reflects a small systematic error possibly incurred during the measurement procedure.

[†]The ellipticity angle of the polarization ellipse is given by $\chi = \frac{1}{2}\sin^{-1}(S_3/S_0)$ for fully polarized light [12].

Table 3.1: Experimental results for nine calibrations with 672.7 nm light using three different quarter-wave plates with design wavelengths denoted by $\lambda_{\pi/2}^{\text{nom}}$, each with three different values of ϕ^{nom}.

ϕ^{nom}		$\lambda_{\pi/2}^{\text{nom}} = 670$ nm	$\lambda_{\pi/2}^{\text{nom}} = 645$ nm	$\lambda_{\pi/2}^{\text{nom}} = 548$ nm
$+3.6°$	β_0	$3.34°$	$3.80°$	$1.16°$
	Δ	$90.47°$	$86.34°$	$75.12°$
	γ	$144.22°$	$144.31°$	$144.21°$
	$\phi - \phi^{\text{nom}}$	$0.85°$	$0.82°$	$0.81°$
$0°$	β_0	$3.55°$	$3.79°$	$1.32°$
	Δ	$90.40°$	$86.28°$	$75.20°$
	γ	$144.29°$	$144.29°$	$144.22°$
	$\phi - \phi^{\text{nom}}$	$0.94°$	$0.82°$	$0.85°$
$-3.6°$	β_0	$3.29°$	$3.78°$	$1.51°$
	Δ	$90.47°$	$86.30°$	$75.09°$
	γ	$144.22°$	$144.30°$	$144.17°$
	$\phi - \phi^{\text{nom}}$	$0.77°$	$0.80°$	$0.87°$
	$\langle\beta_0\rangle$	$3.39(8)°$	$3.787(5)°$	$1.3(1)°$
	$\langle\Delta\rangle$	$90.45(2)°$	$86.31(2)°$	$75.13(3)°$
	$\langle\gamma\rangle$		$144.25(2)°$	
	$\langle\phi - \phi^{\text{nom}}\rangle$		$0.84(2)°$	

Table 3.2: Stokes vectors derived from measurements of horizontally polarized light at 672.7 nm using three different retarders and three intentional misalignments of the retarder vertical rotation axis using the nine calibrations presented in Table 3.1.

ϕ^{nom}	$\lambda_{\pi/2}^{\text{nom}} = 670\text{nm}$	$\lambda_{\pi/2}^{\text{nom}} = 645\text{nm}$	$\lambda_{\pi/2}^{\text{nom}} = 548\text{nm}$
$+3.6°$	$\begin{pmatrix} 1.000 \\ 0.992 \\ 0.120 \\ 0.016 \end{pmatrix}$	$\begin{pmatrix} 1.000 \\ 0.996 \\ 0.116 \\ 0.016 \end{pmatrix}$	$\begin{pmatrix} 1.000 \\ 0.990 \\ 0.128 \\ 0.015 \end{pmatrix}$
$0°$	$\begin{pmatrix} 1.000 \\ 0.998 \\ 0.128 \\ 0.016 \end{pmatrix}$	$\begin{pmatrix} 1.000 \\ 0.998 \\ 0.117 \\ 0.016 \end{pmatrix}$	$\begin{pmatrix} 1.000 \\ 0.992 \\ 0.122 \\ 0.014 \end{pmatrix}$
$-3.6°$	$\begin{pmatrix} 1.000 \\ 0.996 \\ 0.117 \\ 0.017 \end{pmatrix}$	$\begin{pmatrix} 1.000 \\ 1.001 \\ 0.115 \\ 0.017 \end{pmatrix}$	$\begin{pmatrix} 1.000 \\ 0.989 \\ 0.128 \\ 0.016 \end{pmatrix}$

Chapter 4

Literature review - Fabry-Perot interferometers and absorption spectroscopy

Since its conception in 1897 [22], the elegantly simple Fabry-Perot interferometer has been used in a wide range of applications in optical physics including wavemeters, dichroic filters, laser resonators, and of relevance to this project, emission and absorption spectrometers.

Known for their use in recording high-resolution spectra, Fabry-Perot spectrometers have been used to verify the Doppler broadening of emission lines, observe Zeeman splitting and analyze the hyperfine structure of atoms where spectral lines are usually too close together to resolve with conventional spectrometers.

Fabry-Perot elatons came into use in astronomical *absorption* spectroscopy as early as 1927 [23] although with limited success. The chief problem was that slit-pattern distortion produced by the primary dispersive instrument (e.g. a monochromator) would

degrade the resolution of the Fabry-Perot fringe pattern. Primary monochromatization is necessary to limit the spectrum to a wavelength range less than that contained within one period of the repeating fringe pattern produced by the Fabry-Perot etalon (the free spectral range) to avoid overlapping of successive interference orders [24].

The details of combining a pre-monochromator with Fabry-Perot spectrometers were experimented with extensively through the mid-20th century. Treanor reported an order of magnitude improvement in the resolving power attained by a Fabry-Perot configuration coupled with a Littrow spectroscope when analyzing the D region of the solar spectrum [25]. Other attempts to improve resolution included crossing a Fabry-Perot interferometer with a prism monochromator to resolve the rotational structure of HCl in the infra-red [26] and with a grating spectrometer to resolve that of HCN [27]. While offering orders of magnitude higher resolving power in the infra-red region, these configurations were limited to only investigating a small wavelength range of the spectrum of interest at a time since the free spectral range of Fabry-Perot etalons is necessarily small for high-resolution work [28].

Attempts were made to scan the monochromator prism in conjunction with the interferometer plates in order to continously record an extended region of the spectrum, but this was found to be impractical compared to the contemporary innovations of multiple-passing prism and grating spectrometers [29, 30]. Further, this did not provide the ultimate solution as reflection losses reduced the light intensity in multiple-passes [31]. Nonetheless, Fabry-Perot etalons were found to have superior luminosity – the output flux received by a detector – over grating and prism spectrometers for a given resolving power at a particular wavelength and dimension of dispersive element [32].

Absorption spectroscopy is an important tool for identifying the presence of particular molecular species in a sample and quantifying their concentrations. Many techniques are used to obtain the absorption spectrum of a sample but in most cases (with the exception of tunable diode laser absorption spectroscopy) a sample cell or volume is irradiated with broadband light and the transmitted light is measured by a detector. A dispersive element between the sample and the detector decomposes the transmitted light either spatially or temporally into its component frequencies enabling determination of the amount of transmitted light at each frequency. From this information, the absorption spectrum of the sample can be reconstructed and analyzed [33].

We now attempt to understand in more detail the Fabry-Perot interferometer as an absorption spectrometer and determine under what conditions it is useful for providing qualitative and quantitative information about samples under study.

Chapter 5

Fabry-Perot absorption spectroscopy

Currently, analytical devices that detect a single, or small number, of known species are based on chemical reaction or fuel cell technologies due their portability and acceptable level of accuracy. For evidential (quantitative) testing, IR spectroscopy remains the standard analysis technique but is usually restricted to non-portable analysis in a laboratory following a positive screening test. To extend the capability of in-the-field devices to quantitative molecular detection, without the aging issues that currently befall fuel cell-based devices, a portable instrument based on a spectroscopic detection scheme is desired.

The Fabry-Perot interferometer is a compact and robust interferometer design and is capable of high-resolution work with higher luminosity than grating and prism spectrometers for a given resolving power, where luminosity refers to the energy flux output [32]. Fabry-Perot spectroscopy is a well established technique but is commonly

used for *emission* spectroscopy such as resolving hyperfine spectra from atomic emission or studying faint astronomical sources as discussed in Chapter 4. Fabry-Perot *absorption* spectroscopy was superseded more than 40 years ago by other techniques such as multiple-monochromator configurations that offer a similar spectral resolution. However, due to its potential for portability, we wish to revisit the Fabry-Perot as an absorption spectrometer and investigate its feasibility for quantitative detection of ethanol in human breath samples. This involves establishing conditions on the linestrengths and linewidths within the spectrum of interest for which it is useful as an absorption spectrometer using realistic instrumental parameter values. We subsequently attempt to determine if these requirements can be met for the molecule of choice and anticipated concentration.

The strategy adopted in this chapter is as follows: First, a mathematical description of the Fabry-Perot interferometer, that incorporates the effects of non-monochromatic incident light sources and inevitable manufacturing imperfections, will be given followed by simulations of its transmission function for varying *instrumental* parameters such as the bandwidth of the light source and quality of the interferometer's surfaces. Second, the basic principles of absorption spectroscopy, namely Beer's Law, will be introduced to guide the reader through the details of the absorption spectrum of a human breath sample containing water and ethanol vapours. This will provide a basis for outlining the detection scheme and subsequently establishing its *spectroscopic* requirements. Third, a new concept for a portable, optical breathalyzer will be outlined as a possible application for the proposed detection scheme.

5.1 Fabry-Perot interferometry

5.1.1 The ideal Fabry-Perot interferometer

A Fabry-Perot interferometer is based on interference between co-propagating plane waves reflected from two parallel highly-reflecting surfaces and therefore falls into the category of multiple interference devices. When a resonance condition is met, defined by refractive index between the surfaces, n, and their separation, d, as well as the angle of internal reflection, θ, and wavelength, λ, of monochromatic light entering the interferometer, constructive interference produces a bright fringe that is visible on a screen placed behind the interferometer. If the incident light is composed of a *set* of monochromatic lines, several resonance conditions exist producing a repeating series of fringes. The resonance condition is met when the phase difference between the co-propagating plane waves, δ, i.e. the round trip phase difference:

$$\delta = \frac{4\pi n d \cos\theta}{\lambda} \tag{5.1}$$

is equal to an integer multiple of 2π. The interference or fringe order (i.e. the number of full periods of phase difference between adjacent reflected rays) is correspondingly:

$$m = \frac{\delta}{2\pi} = \frac{2nd\cos\theta}{\lambda}. \tag{5.2}$$

Scanning n, d, θ or λ in time effectively scans δ, producing a *temporal* variation in intensity when the transmitted (or reflected) rays are focused onto a detector with a lens. A Fabry-Perot interferometer with a fixed d – commonly a solid slab with refractive index n – is known as an *etalon*. For this configuration θ is related to the

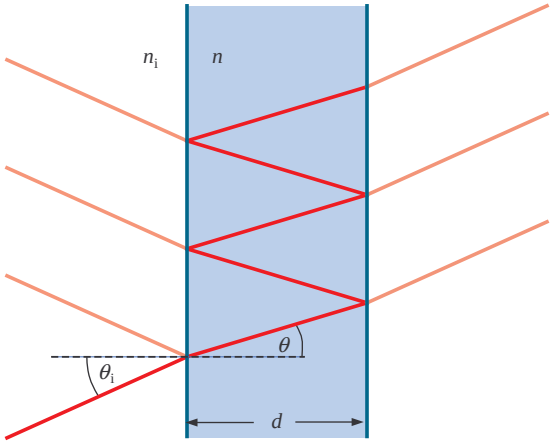

Figure 5.1: Illustration of a solid Fabry-Perot etalon of refractive index n and thickness d with a monochromatic light beam incident at θ_i. The refractive index outside the etalon is n_i and θ is the angle of internal reflection.

angle of incidence of collimated light entering the etalon, θ_i, by Snell's law:

$$n \sin\theta = n_i \sin\theta_i, \tag{5.3}$$

where n_i is the refractive index outside the etalon (see Fig. 5.1). If the incident light enters the interferometer with a range of angles, i.e. the light is non-collimated, a *spatial* fringe pattern of bright and dark concentric rings is produced on a screen placed behind the interferometer.

The power transmission function of an ideal etalon with homogeneous absorption and/or scattering by the material that comprises the etalon and monochromatic incident light is given by [34]:

$$Y(\delta) = \frac{A\,(1-R)^2}{1 - 2R\cos\delta + R^2} \tag{5.4a}$$

$$= \frac{A}{1 + \left[4R\,(1-R)^{-2}\right]\sin^2(\delta/2)}, \tag{5.4b}$$

where A includes the absorption and/or scattering effects and R is the reflectivity of the etalon given by the product of the reflection coefficient of each surface. Eq. (5.4b) is known as the Airy function.

It is apparent that constructive interference fringes are spaced by 2π in δ-space. If a second monochromatic source is introduced, its wavelength relative to the first can be unambiguously determined if the difference in wavelength between them is less than the *free spectral range* of the etalon. The difference in wavelength at which the n^{th} fringe produced by the second source overlaps with the $(n+1)^{\text{th}}$ fringe produced by the first defines the free spectral range. In terms of wavenumber ($\tilde{\nu} \equiv \lambda^{-1}$) the free spectral range is:

$$\Delta\tilde{\nu}_{fsr} = \frac{1}{2nd\cos\theta}. \tag{5.5}$$

In other words, the free spectral range is the spectral window that can be seen in one period of the produced fringe pattern. For spectroscopic work using a Fabry-Perot etalon, it is necessary to limit the total width of the spectrum one wishes to investigate to less than the etalon's free spectral range by using a narrowband source, band-pass filter or pre-monochromator to avoid overlapping of spectral orders. The free spectral range can also be defined in terms of the difference between adjacent interference orders in the other scannable parameters (n, d, θ), indicating the tuning range beyond which a fringe pattern is necessarily expected to repeat. For example:

$$\Delta d_{fsr} = \frac{1}{2n\tilde{\nu}\cos\theta} \tag{5.6}$$

is the tuning range of d between adjacent orders.

Similarly, the full width at half maximum (FWHM) of each interference fringe can

be expressed in terms of any of the scannable parameters. For an ideal etalon with monochromatic light, the FWHM of fringes in terms of δ is given by:

$$\Delta\delta = 4\sin^{-1}\left[\frac{1-R}{2\sqrt{R}}\right] \approx \frac{2(1-R)}{\sqrt{R}}, \tag{5.7}$$

where the approximation shown in (5.7) and the next three equations is valid when $R \approx 1$.

The ratio of the free spectral range to the FWHM of fringes is called the *finesse*, $\mathcal{F}$. This ratio is independent of the scannable parameters so it is a useful metric for describing the quality of an etalon. The finesse of an ideal etalon, known as the *reflective finesse*, is solely dependent on the reflectivity of the surfaces and increases rapidly as R approaches 1:

$$\mathcal{F} = \frac{\Delta\delta_{fsr}}{\Delta\delta} = \frac{\pi}{2\sin^{-1}\left[(1-R)\left(2\sqrt{R}\right)^{-1}\right]} \approx \frac{\pi\sqrt{R}}{1-R}. \tag{5.8}$$

The *resolving limit* or *spectral resolution* is defined according to the Rayleigh criterion as follows: two equal intensity peaks are said to be resolved or clearly distinguishable from each other when their separation is equal to their FWHM and so the resolving limit is given by the FWHM of fringes. In terms of wavenumber, or indeed any of the scannable parameters, this can be derived from the finesse of the etalon and the appropriate representation of the free spectral range. For example:

$$\Delta\tilde{\nu} = \frac{\Delta\tilde{\nu}_{fsr}}{\mathcal{F}} = \frac{\sin^{-1}\left[(1-R)\left(2\sqrt{R}\right)^{-1}\right]}{\pi nd\cos\theta} \approx \frac{(1-R)R^{-1/2}}{2\pi nd\cos\theta}. \tag{5.9}$$

In contrast to the finesse, the *resolving power*, $\mathcal{R}$, is dependent on the wavenumber

of the incident light and is equivalently defined in terms of any of the scannable parameters:

$$\mathcal{R} = \frac{\tilde{\nu}}{\Delta\tilde{\nu}} = \frac{n}{\Delta n} = \frac{d}{\Delta d} = \frac{\cos\theta}{\Delta\cos\theta} = \frac{\pi\tilde{\nu}nd\cos\theta}{\sin^{-1}\left[(1-R)\left(2\sqrt{R}\right)^{-1}\right]} \approx \frac{2\pi\tilde{\nu}nd\cos\theta}{(1-R)R^{-1/2}}. \tag{5.10}$$

An $\mathcal{R}$ value of 10^6 or more is indicative of a 'good' Fabry-Perot interferometer for a given light source.

5.1.2 Non-monochromatic sources

In practice, for any set of instrumental parameters the response function of a Fabry-Perot etalon is broadened by finite-linewidth light sources. In conventional Fabry-Perot emission spectroscopy, the finite linewidth of spontaneous emission due to natural lifetime broadening (Lorentzian lineshape) and Doppler broadening (Gaussian lineshape) results in broadening of interference fringes further than that given by Eq. (5.7).

The effects of non-monochromatic sources can be incorporated into the resultant interference pattern by adding together a set of ideal etalon responses with an intensity distribution in the form of the appropriate lineshape [35]. If the lineshape is symmetric, the mathematical operation that describes this is the *convolution* integral. The convolution $h(x)$ of two symmetric functions, $f(x)$ and $g(x)$, is given by:

$$h(x) = f * g = \int_{-\infty}^{\infty} f(y)g(x-y)dy. \tag{5.11}$$

This operation can be pictured as inverting one function and sliding it across the other,

computing the product of the two functions at each step. In general (for asymmetric functions) the cross-correlation integral, which instead involves $g(x+y)$, describes the above operation but for convenience the convolution is widely used where possible. The convolution owes its convenience of use to its commutativity, associativity and distributivity – properties that are not shared by the cross-correlation. Analytic solutions to convolutions of (a) Gaussian, (b) Lorentzian and (c) top hat (boxcar) functions with the ideal etalon response function are presented below with derivations for each one given in Appendix A:

(a) The functional form of a unit area Gaussian source profile, $S_G(x)$, centred at $x = 0$ with FWHM Δx_G is given by:

$$S_G(x) = \frac{1}{\sqrt{\pi}\,G}\, e^{-x^2/G^2}, \qquad \Delta x_G = 2\sqrt{\ln 2}\, G, \tag{5.12}$$

and examples plotted in terms of phase angle, δ, for different values G are shown in Fig. 5.2(a). The convolution of a Gaussian profile written in terms of δ with the ideal etalon response function is as follows:

$$\begin{aligned} Y_G(\delta) = S_G * Y &= \int_{-\infty}^{\infty} S_G(y) Y(\delta - y) dy \\ &= \frac{1-R}{1+R}\left[1 + 2\sum_{k=1}^{\infty} R^k e^{-k^2 G^2/4} \cos k\delta\right]. \end{aligned} \tag{5.13}$$

Eq. (5.13) can be used to determine the interference pattern produced by an etalon illuminated by a light source with a Gaussian spectral profile as a function of δ [as has been done in Fig. 5.2(b)] or any of the scannable parameters through an appropriate

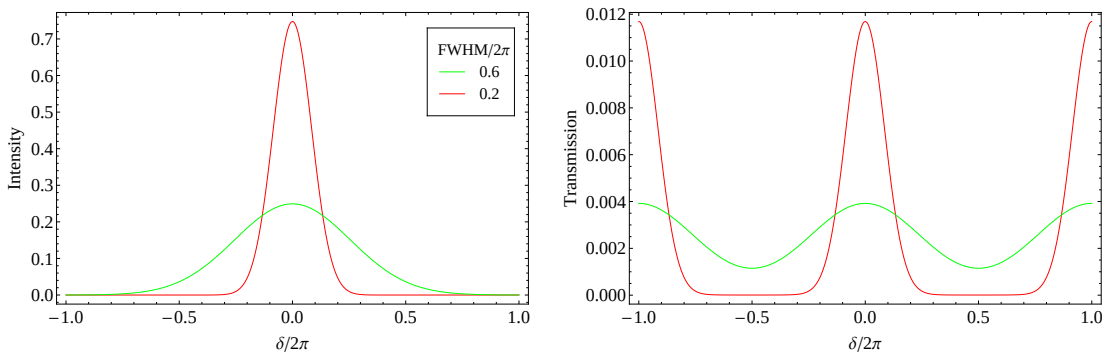

(a) (b)

Figure 5.2: (a) Gaussian source profiles and (b) corresponding etalon responses for $R = 0.995$.

variable transformation.

(b) A unit area Lorentzian source profile, $S_L(x)$, centred at $x = 0$ with FWHM Δx_L is given by:

$$S_L(x) = \frac{L}{\pi}\frac{1}{L^2 + x^2}, \qquad \Delta x_L = 2L, \tag{5.14}$$

and is shown plotted in terms of δ for different values of L in Fig. 5.3(a). The convolution of a Lorentzian profile with the ideal etalon response function is as follows:

$$\begin{aligned} Y_L(\delta) = S_L * Y &= \int_{-\infty}^{\infty} S_L(y) Y(\delta - y) dy \\ &= \frac{1-R}{1+R}\left[1 + 2\sum_{k=1}^{\infty}(Re^{-L})^k \cos k\delta\right], \end{aligned} \tag{5.15}$$

Similarly, the fringe pattern produced by a Lorentzian light source (e.g. spontaneous emission in the absence of Doppler broadening) incident on an ideal etalon can be determined using Eq. (5.15). Examples of this are illustrated in Fig. 5.3(b).

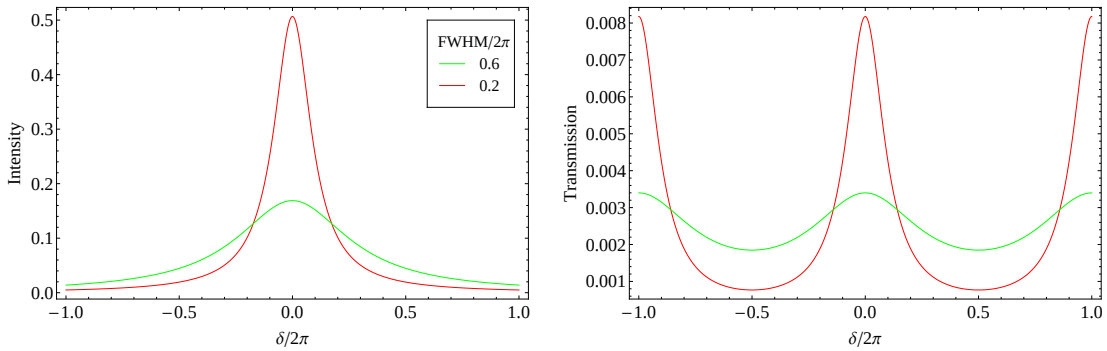

(a) (b)

Figure 5.3: (a) Lorentzian source profiles and (b) corresponding etalon responses for $R = 0.995$.

(c) A unit area top hat source function of width W centred at $x = 0$ is given by:

$$S_\Pi(x) = \frac{1}{W}\,\Pi_W(x), \qquad \Pi_W(x) = \begin{cases} 1, & |x| \le W/2 \\ 0, & |x| > W/2 \end{cases}, \tag{5.16}$$

with examples plotted in terms of δ for different values of W illustrated in Fig. 5.4(a). The convolution of this profile with the ideal etalon response function is:

$$\begin{aligned} Y_\Pi(\delta) = S_\Pi * Y &= \int_{-\infty}^{\infty} S_\Pi(y) Y(\delta - y)\,dy \\ &= \frac{1-R}{1+R}\left[1 + 2\sum_{k=1}^{\infty} R^k \operatorname{sinc}(kW/2)\cos k\delta\right], \end{aligned} \tag{5.17}$$

where $\operatorname{sinc} x = \sin x/x$. A top hat function can approximate a source resulting from reflecting broadband light from a dielectric mirror with a large number of dielectric layers. The transmission of such a profile through an ideal etalon as a function of δ can be determined using Eq. (5.17) as is shown in Fig. 5.4(b).

Upon inspection of the analytic solutions of these convolutions, the reader can

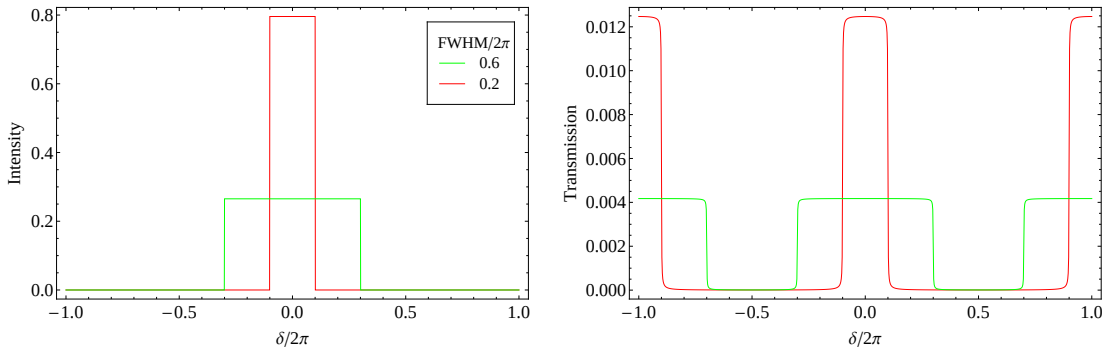

(a) (b)

Figure 5.4: (a) Top hat source profiles and (b) corresponding etalon responses for $R = 0.995$.

identify the following general form for an output $Y'(\delta)$ from an incident profile written in terms of phase angle, $S(\delta)$:

$$Y'(\delta) = S * Y = \frac{1-R}{1+R}\left[1 + 2\sum_{k=1}^{\infty} R^k s_k \cos k\delta\right], \tag{5.18}$$

where s_k is the Fourier transform of $S(\delta)$, following from the convolution theorem as described by Boas in [36]. As the width of the source is increased from a monochromatic line to a finite width profile, the etalon response is broadened while fringe maxima decrease and minima increase towards a flat transmission function:

$$Y'_{\text{white}} = \frac{1-R}{1+R}, \tag{5.19}$$

for 'white' or very broad-band light. Some examples of this mapped onto frequency space using realistic linewidth values are illustrated in Fig. 5.5 for Gaussian and top hat source profiles. Regardless of their functional forms, both demonstrate the same broadening behaviour toward the Y'_{white} limit as the FWHM approaches and exceeds the free spectral range of the etalon.

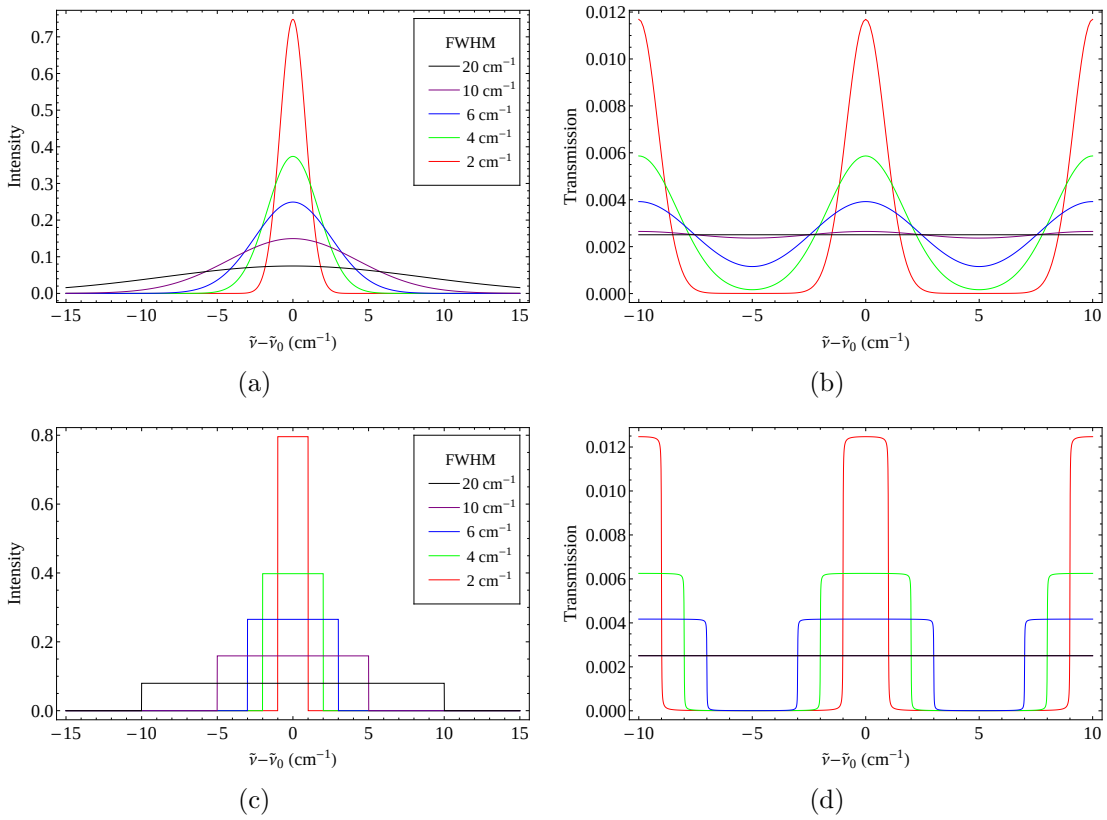

Figure 5.5: (a) Gaussian and (c) top hat source profiles and (b) & (d) corresponding ideal etalon responses for $R = 0.995$ and $\Delta\tilde{\nu}_{fsr} = 10\,\mathrm{cm}^{-1}$. For FWHMs $\gtrsim \Delta\tilde{\nu}_{fsr}$, the transmission approaches Y_{white}.

5.1.3 Non-ideal etalons

Two aspects of a Fabry-Perot etalon that further broaden its fringe pattern are rough or non-parallel reflective surfaces. If these imperfections can be modeled by Gaussian, Lorentzian or top hat profiles, the convolutions above can be used to include their effects on the etalon response. Provided any microscopic imperfections in flatness are randomly distributed and the resulting variation in etalon surface spacing is much smaller than d, a single etalon can be treated as a collection of ideal etalons with a normal distribution of surface spacings. Under these assumptions, flatness

imperfections can be modelled by a Gaussian profile $D_F(\delta)$ with FWHM $\Delta\delta_F$:

$$D_F(\delta) = \frac{1}{\sqrt{\pi}\,F}\,e^{-\delta^2/F^2}, \qquad \Delta\delta_F = 2\sqrt{\ln 2}\,F. \tag{5.20}$$

An expression for F for a particular variation in surface spacing due to roughness, Δd_F, can be found by differentiating Eq. (5.1) with respect to d, substituting the expression for $\Delta\delta_F$ from Eq. (5.20) and solving for F:

$$F = \frac{2\pi\tilde{\nu}n\cos\theta}{\sqrt{\ln 2}}\Delta d_F. \tag{5.21}$$

Additionally, provided the variation in etalon surface spacing due to an error in parallelism across the illuminated area is much smaller than d, spherically-curved or non-parallel surfaces due to imperfect polishing of the etalon slab can be treated as a collection of ideal etalons with a flat distribution of surface spacings. This type of variation can be expressed by a top hat function [37]:

$$D_P(\delta) = \frac{1}{P}\Pi_P(\delta), \qquad \Pi_P(\delta) = \begin{cases} 1, & |\delta| \le P/2 \\ 0, & |\delta| > P/2 \end{cases} \tag{5.22}$$

where P is the width in δ-space of the top hat profile representing the curvature/non-parallel aspect of the etalon surfaces. An expression for P for a particular variation in surface spacings due to non-parallel surfaces, Δd_p, is given by:

$$P = 4\pi n\tilde{\nu}\cos\theta\Delta d_P. \tag{5.23}$$

For example, the response of a non-ideal etalon (assumed to have rough, denoted by

F, *and* non-parallel, denoted by P, surfaces) to an input source with a Lorentzian intensity profile, $S_L(\delta)$ is given by the convolution of the appropriate profiles with the etalon transmission function, $(Y(\delta))$:

$$\begin{aligned} T(\delta) &= S_L * D_F * D_P * Y \\ &= \frac{1-R}{1+R}\left[1 + 2\sum_{k=1}^{\infty}\left(Re^{-L}\right)^k e^{-k^2F^2/4}\mathrm{sinc}(kP/2)\cos k\delta\right]. \end{aligned} \tag{5.24}$$

The broadening effects of a non-monochromatic source together with surface imperfections reduce the effective finesse of the etalon and therefore degrade the resolution and visibility of fringes. These effects can be minimized by making R as close to 1 as possible but nonetheless these effects limit the physically achievable resolution and fringe visibility. It is important to note that fringe broadening associated with a non-monochromatic light source does *not* apply to absorption features within the source profile. The ability to resolve these features is, however, affected by the broadening associated with etalon imperfections.

5.1.4 Analysis of fringe visibility

One measure of fringe contrast for an ideal etalon analyzing monochromatic light which is independent of the average intensity of the light is the *visibility*, V:

$$V \equiv \frac{Y_{\max} - Y_{\min}}{Y_{\max} + Y_{\min}} = \frac{2R}{1+R^2}, \tag{5.25}$$

which is a value that can vary from 0 to 1 and is enhanced for larger values of $Y_{\max}/Y_{\min}$. For an ideal etalon analyzing non-monochromatic light, $Y_G(\delta)$, for example, must be evaluated at $\delta = 0$ and $\delta = \pi$ to obtain $Y_{\max}$ and $Y_{\min}$, respectively. The

dependence of V on the source width for a particular set of instrumental parameters for an ideal etalon is illustrated in Fig. 5.6 for various source profiles.

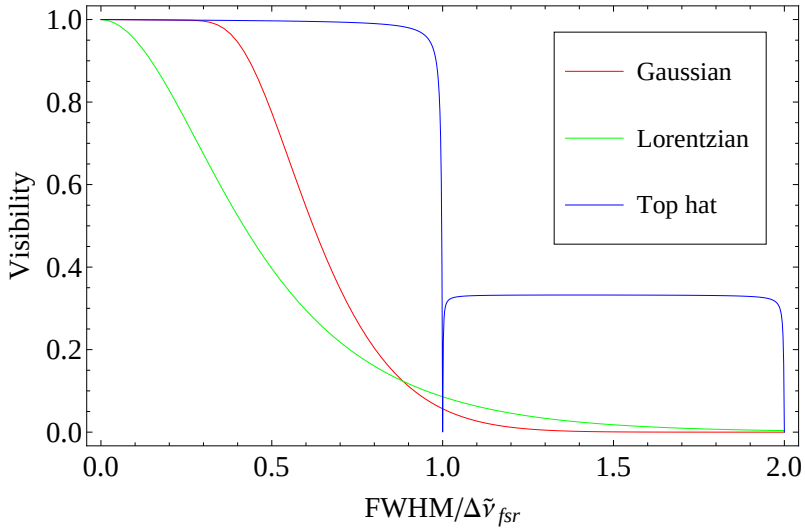

Figure 5.6: Visibility of fringes produced by an ideal etalon with various source profiles of varying widths given by their FWHM value relative to the free spectral range for $R = 0.995$ and $\Delta\tilde{\nu}_{fsr} = 10\,\mathrm{cm}^{-1}$. The non-zero visibility of the top hat profile for FWHMs $> \Delta\tilde{\nu}_{fsr}$ results from a distinct type of fringe pattern due to the discrete nature of the leakage of light intensity into adjacent interference orders.

5.2 Application to absorption spectroscopy

Fabry-Perot spectroscopy is commonly used for high-resolution studies such as recording hyperfine emission spectra and low-resolution spectroscopy of very faint cosmic sources. We wish to investigate its applicability for measuring *absorption spectra* of human breath samples containing water and ethanol vapour. The feasibility of this application hinges on: a) whether the spectral resolution of the device is sufficient to resolve absorption features in the wavenumber region of interest and b) whether the intensity resolution is sufficient to resolve small changes in the relative absorption

intensity of these features.

If the incident light source contains narrow absorption features, these can be spectrally resolved with the same resolution as emission peaks [25] although with significantly reduced intensity visibility. We have modelled the response of an ideal, and non-ideal, Fabry-Perot spectrometer with non-monochromatic sources of varying widths containing absorption features to determine how the resulting visibility depends on the source width and the width and depth of the absorption features. The motivation for this was to determine whether small changes in the relative depths of water vapour absorption features corresponding to the presence of different levels of ethanol concentration could be resolved by a compact angle-resolved Fabry-Perot optical spectrum analyzer [38]. Although Fabry-Perot spectroscopy has not been widely-used for absorption spectroscopy in the past, the sensitivity of modern detectors could indeed permit high enough resolution in intensity for detecting the presence of ethanol.

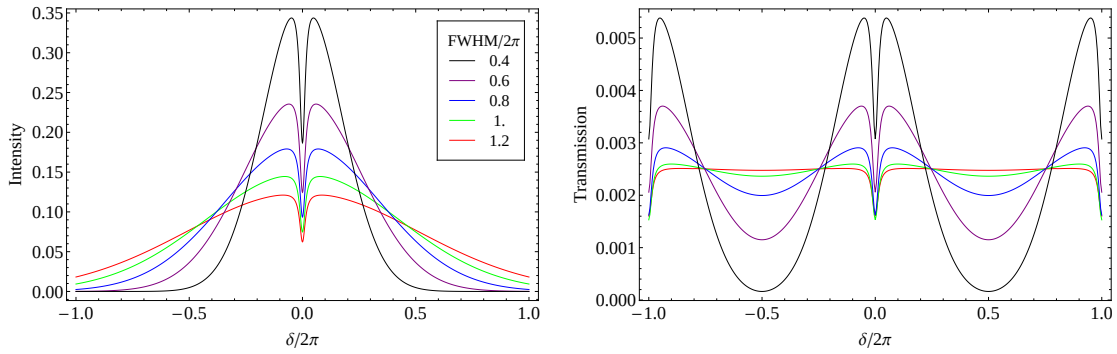

(a) (b)

Figure 5.7: (a) Gaussian source profiles of varying widths given by FWHM/2π containing a 0.25 cm^{-1} FWHM absorption feature with 50% transmittance. (b) The resulting fringe pattern of an ideal etalon with $R = 0.995$ with source profiles shown in (a).

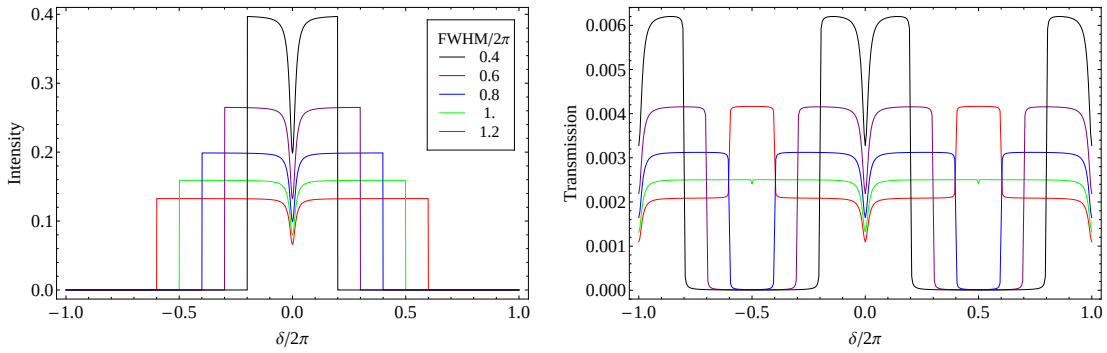

(a) (b)

Figure 5.8: (a) Top hat source profiles of varying widths given by FWHM/2π containing a 0.25 cm^{-1} FWHM absorption feature with 50% transmittance. (b) The resulting fringe pattern of an ideal etalon with $R = 0.995$ with source profiles shown in (a). The 'step' in transmission near $\delta = \pm\pi$ for a top hat source with FHWM/$2\pi = 1.2$ occurs due to the discrete nature of the leakage of light intensity into adjacent interference orders.

A single absorption feature with a Lorentzian lineshape was introduced with assumed Gaussian and top hat source profiles using Beer's law (see section 5.3.1 below for details), that is, using Eq. (5.14) in Eq. (5.28) with I_0 as a function of δ taking the form of Eqs. (5.12) and (5.16), respectively. Convolutions of source profiles containing an absorption feature with the etalon response were performed numerically as analytic solutions were not readily available. For example, the transmission of an ideal etalon with a Gaussian source profile containing an absorption feature, $T_\alpha(\delta)$, as shown in Fig. 5.7(b) for various source widths, is given by:

$$T_\alpha(\delta) = S_G\, e^{-aS_L} * Y = \int_{-\infty}^{\infty} S_G(y) e^{-aS_L(y)} Y(\delta - y) dy, \tag{5.26}$$

where the value of the prefactor, a, was chosen such that the incident intensity dropped to 50% of the peak value of S_G at the centre of the absorption feature in Fig. 5.7(a). Top hat source profiles containing a Lorentzian absorption feature and

the corresponding ideal etalon responses were modelled in a similar fashion and are shown in Fig. 5.8.

The transmission of a non-ideal etalon with rough surfaces with a Gaussian incident source containing a Lorentzian absorption feature, $T'_\alpha(\delta)$, is given by:

$$T'_\alpha(\delta) = D_G * S_G\, e^{-aS_L} * Y = \int_{-\infty}^{\infty} D_G(z) S_G(y-z) e^{-aS_L(y-z)} Y(\delta - y) dy dz. \quad (5.27)$$

The broadening effects due to rough etalon surfaces on the resulting fringe pattern are demonstrated in Fig. 5.10 for different source widths and different amounts of surface roughness.

5.2.1 Visibility of absorption features

The visibility of an absorption feature *within* a source profile is not such a straightforward calculation to do as the phase angle corresponding to the maximum transmission is not obvious *a priori*. The position of $T_{\alpha,\max}$ depends on the FWHM of the absorption feature relative to that of the source and also on the lineshape of the source. In addition to this, the relevant minimum is at the centre of the absorption feature and not necessarily the global minimum at $\delta = \pi$.

The visibility of absorption features depends primarily on the width of the source relative to the free spectral range as shown in Fig. 5.9. Reducing the source width improves the visibility but the spectral window that can be investigated is consequently also decreased. The source width must therefore be wide enough to capture a large enough spectral window to investigate ratios of absorption intensities but narrow enough to ensure sufficient visibility to detect changes in these ratios.

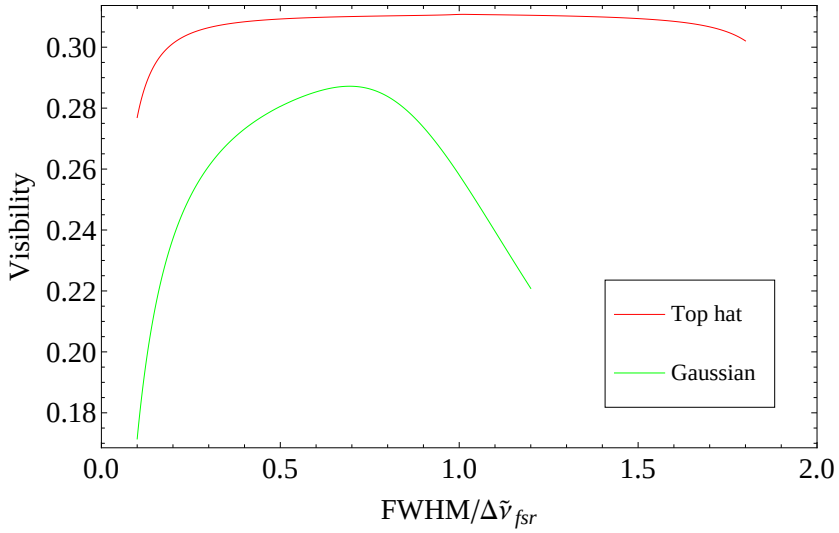

Figure 5.9: Visibility of absorption features within fringes produced by an ideal etalon with two source profiles of varying widths given by their FWHM value relative to the free spectral range for $R = 0.995$ and $\Delta\tilde{\nu}_{fsr} = 10\,\mathrm{cm}^{-1}$. The source profiles contain a $0.25\,\mathrm{cm}^{-1}$ FWHM absorption feature with 50% transmittance.

The standard approach to avoiding overlapping orders in one free spectral range is to use a monochromator or grating spectrometer to send only one order with a spectral width comparable to the free spectral range to the etalon [28]. We are considering a compact, less expensive approach involving a narrow-band light source such as an LED with a band-pass filter. Commercially available Bragg-grating reflection filters with very narrow pass-bands could be used for this purpose [39].

Absorption feature visibility also depends on broadening mechanisms such as decreased reflectivity and etalon imperfections – in other words, the effective finesse. These compounding effects are qualitatively illustrated in Fig. 5.10 for source widths much less than the free spectral range with $R = 0.99$ and random flatness imperfections $<< d$.

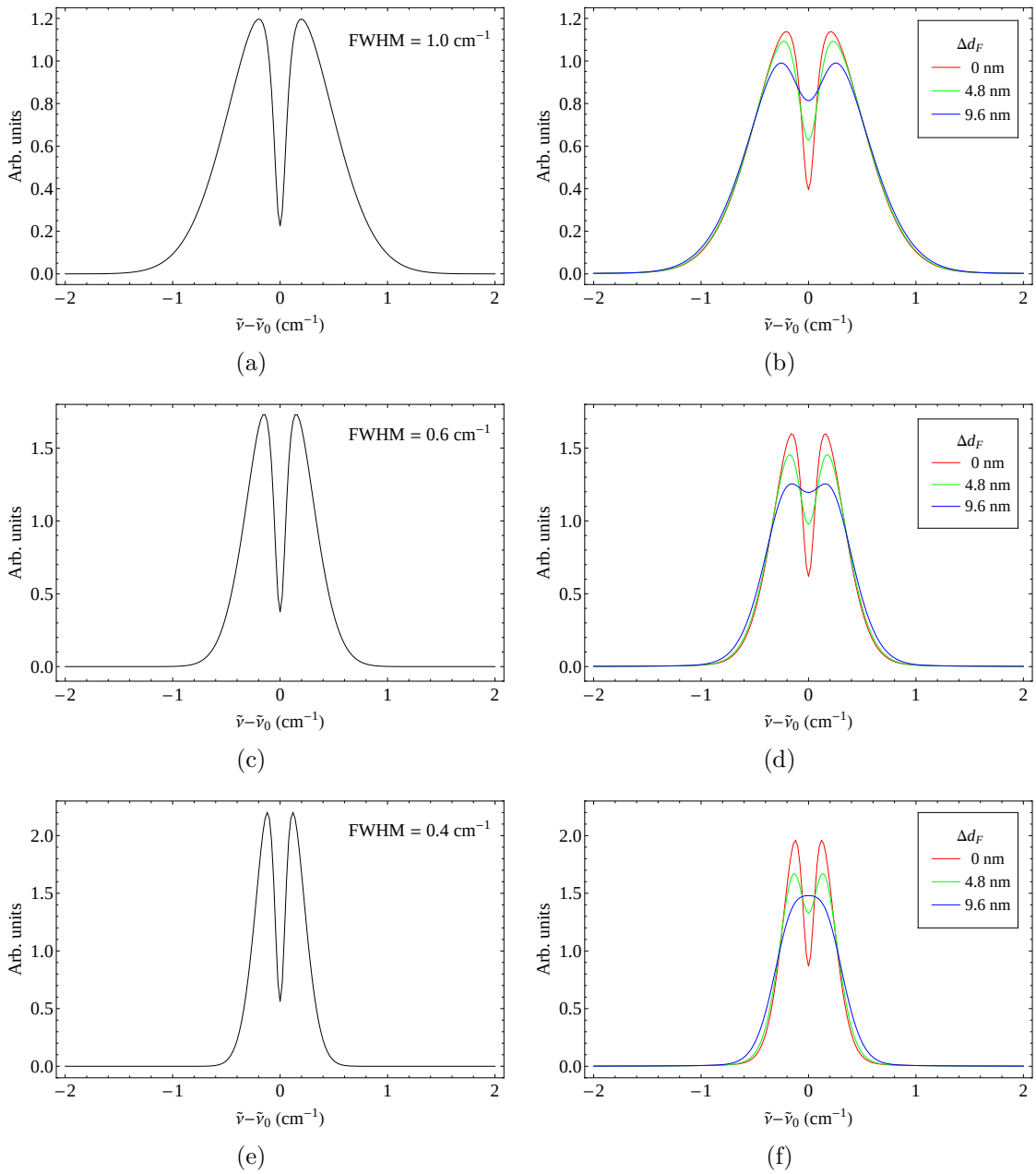

Figure 5.10: Gaussian source profiles with (a) $1.0\,\mathrm{cm}^{-1}$ (c) $0.6\,\mathrm{cm}^{-1}$ and (e) $0.4\,\mathrm{cm}^{-1}$ FWHMs containing a $0.25\,\mathrm{cm}^{-1}$ FWHM absorption feature with 15% transmittance. (b), (d) & (f) Resulting fringe patterns of ideal and non-ideal etalons with surface roughness given by d_F corresponding to the input profiles in (a), (c) & (e), respectively, for $R = 0.99$ and $\Delta\tilde{\nu}_{fsr} = 10\,\mathrm{cm}^{-1}$. Source profiles and etalon responses are normalized to unit area for comparison.

5.3 Quantitative spectroscopy of ethanol

Molecules can absorb energy in the form of electromagnetic radiation that is resonant with transitions between rovibronic states, i.e. when the photon energy (which is proportional to the frequency of the electromagnetic wave) is equal to the energy difference between two states. The dominant mechanism that allows the molecule to absorb energy is the interaction between the electric dipole moment produced by the configuration of charged particles that the molecule is composed of and the oscillating electric field of the electromagnetic wave. Upon absorbing a photon, the molecule is excited to the upper (higher) energy state where it remains until it decays back to a lower energy state through collisions or via spontaneous or stimulated emission by emitting a photon of the same energy. Each molecule has a unique set of energy states based on its composition (number and types of component atoms), structure (number and types of inter-atomic bonds) and configuration (spatial orientation of atoms and bonds) and thus can support a unique set of transitions. Each of these transitions has a strength associated with it depending on the probability of that transition, and the total set of transition frequencies and associated strengths at a given temperature provides a unique fingerprint or *spectrum* of that molecular species.

Spectroscopy is the study of atomic and molecular spectra and therefore the study of the interaction of light with matter. Different regions of the electromagnetic spectrum are generally associated with different types of interactions. Here, we concentrate on infrared radiation ($33.3\,\mathrm{cm}^{-1}$ to $12\,800\,\mathrm{cm}^{-1}$; $300\,\mu\mathrm{m}$ to $780\,\mathrm{nm}$) which tends to drive vibrational transitions in matter.

5.3.1 Beer's Law

Beer's law describes the light intensity transmitted through an absorbing material as a function of wavenumber:

$$I(\tilde{\nu}) = I_0 e^{-\alpha(\tilde{\nu})L}, \tag{5.28}$$

where I_0 is the incident light intensity at $\tilde{\nu}$, $I(\tilde{\nu})$ is the transmitted intensity, $\alpha(\tilde{\nu})$ is the absorption coefficient at that wavenumber and L is the path length of the light in the absorbing material. The ratio of transmitted to incident light intensity, I/I_0, is known as the transmittance while $\ln(I_0/I)$ is the absorbance. The absorption coefficient of a particular transition in a species from lower state η to upper state η' at temperature T and pressure p, $\alpha_{\eta\eta'}(\tilde{\nu}, T, p)$ [in cm^{-1}], is the product of the line intensity, $S_{\eta\eta'}(T)$ [in $\text{cm}^{-1}/(\text{molecule cm}^{-2})$], and lineshape, $g(\tilde{\nu} - \tilde{\nu}_{\eta\eta'}, T, p)$ [in cm^{-1}], of that particular transition and the concentration, N [in molecules/cm^3], of absorbing molecules:

$$\alpha_{\eta\eta'}(\tilde{\nu}, T, p) = S_{\eta\eta'}(T) g(\tilde{\nu} - \tilde{\nu}_{\eta\eta'}, T, p) N. \tag{5.29}$$

This can also be expressed in terms of the per molecule absorption, or absorption cross-section, of a particular transition, $\sigma_{\eta\eta'}(\tilde{\nu}, T, p)$ [in cm^2/molecule], given by:

$$\sigma_{\eta\eta'}(\tilde{\nu}, T, p) = S_{\eta\eta'}(T) g(\tilde{\nu} - \tilde{\nu}_{\eta\eta'}, T, p). \tag{5.30}$$

Therefore, measurement of the absorbance at a particular frequency of a fixed path length of molecules held at a fixed temperature and pressure allows one to determine the concentration if the total absorption cross-section at that frequency is known.

This is the basis of *quantitative* absorption spectroscopy.

Line intensities tabulated at a reference temperature in databases such as *HITRAN* [40] are derived from experimental data or from *ab initio* calculations. The lineshape of a single transition is in general a Voigt profile resulting from the convolution of Lorentzian and Gaussian profiles due to homogeneous and inhomogeneous broadening mechanisms such as pressure and Doppler broadening, respectively. In lower-atmospheric studies, pressure broadening dominates so a Lorentzian profile is assumed. The Lorentzian half-maximum half-widths at standard temperature and pressure are also tabulated in *HITRAN* along with the lower state energies. With this information and an assumed concentration the spectrum of a molecular species sample can be simulated by plotting the total absorption coefficient associated with all transitions as a function of wavenumber:

$$\alpha(\tilde{\nu}, T, p) = \sum_{\eta\eta'} \alpha_{\eta\eta'}(\tilde{\nu}, T, p). \tag{5.31}$$

5.3.2 Ethanol vapour spectrum: O-H stretch overtones

The overtones of the O-H stretch vibration of many organic molecules have been extensively studied by atmospheric chemists [41]. Ethanol (EtOH; CH_3–CH_2–OH) is a large, floppy molecule and therefore has broad vibrational bands in its spectrum. Rotation about its CO bond leads to two rotational conformers: *trans*- when the methyl group (CH_3–) is across from the OH bond and *gauche*- when the OH bond is across from one of the CH bonds of the methylene group (–CH_2–).

Theoretical results based on density functional theory (DFT) calculations [42] and experimental results using photoacoutic spectroscopy (PAS) [43] show that the O-H

stretch vibration overtones of *trans*-ethanol have larger transition energies and slightly stronger absorption intensities than those of the *gauche*-conformer. The *trans*-ethanol O-H overtones also show a strong Q-branch peak [43] in experimental spectra. This absorption feature is desirable for quantitative spectroscopy and detection due to its relative sharpness compared to the other broader rotational branches (P- and R-). In particular, the second overtone centred at $\sim 10\,500\,\mathrm{cm}^{-1}$ lies in the near-IR region ($3333\,\mathrm{cm}^{-1}$ to $12\,800\,\mathrm{cm}^{-1}$; $3\,\mu\mathrm{m}$ to $780\,\mathrm{nm}$) where affordable sources and detectors exist. Integrated absorption intensities and centres of entire O-H stretch overtone bands have been calculated from FTIR and near-IR spectra in [44] for ethanol and similar species containing an isolated O-H bond. These results, along with an experimental spectrum from [43] [shown in Fig. 5.11(a)] have been used to estimate the absorption cross-section of *trans*-ethanol's Q-branch ($\approx 10\,515\,\mathrm{cm}^{-1}$; $\approx 951\,\mathrm{nm}$) in the second O-H stretch overtone band.

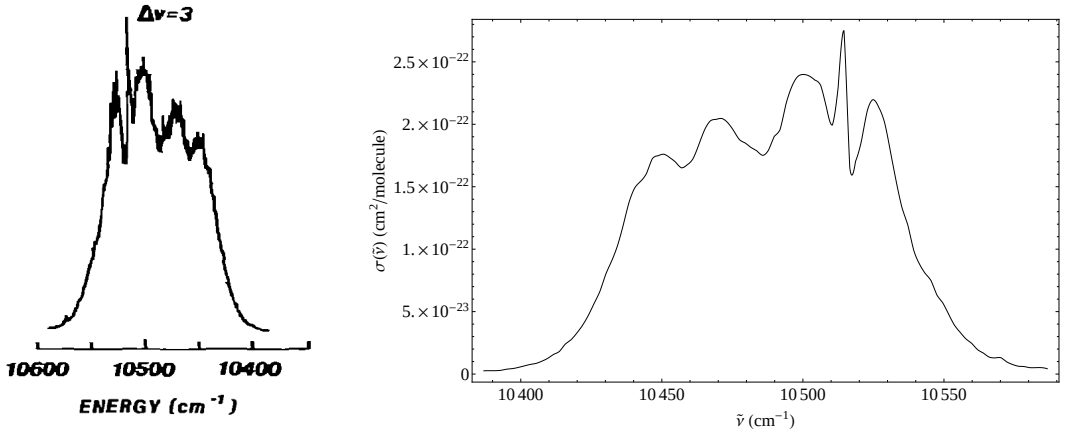

(a) (b)

Figure 5.11: (a) Experimental absorption spectrum of v_{OH3} vibrational band in EtOH from [43]. (b) Estimated absorption cross-section using the value $I_{03} = 2.24 \times 10^{-20}$ cm/molecule from [44] for the band intensity of v_{OH3} in EtOH.

The absorption coefficient includes the concentration, N, of the absorbing species.

The number density of ethanol molecules in a human breath sample is related to the breath alcohol content (BrAC) in milligrams per litre (mg/l) of breath by Avagadro's number. BrAC is related to blood alcohol content (BAC) through the accepted ratio of 1 : 2100 in Canada and the US. BAC units are defined such that 0.01% BAC = 100 mg/l blood. For simplicity the notation 1 'BAC' ≡ 0.001% BAC will be used henceforth. Legal limits of consumed alcohol for motor vehicle operators are given in terms of BAC. The legal limit in Canada of 50 BAC corresponds to 127 ppm (0.238 mg/l) of ethanol in expired breath at standard temperature and pressure while an anticipated minimum detectable amount of 4 BAC similarly corresponds to 10 ppm (0.019 mg/l). In what follows, the absorption coefficient of ethanol has been estimated at these concentrations (Section 5.3.4).

5.3.3 Water vapour spectrum simulated from *HITRAN*

Water (H_2O) is a light, rigid molecule and in its vapour state it has a complex spectrum with more than 64 000 tabulated absorption lines ranging from the visible to the microwave region of the electromagnetic spectrum. This data is compiled at a reference temperature (296 K) and pressure (1 atm) in the *HITRAN* database along with that from forty other molecular species commonly found in the earth's atmosphere. The water vapour spectrum in the region of ethanol's Q-branch of the first and second O-H stretch overtones at 7170 cm^{-1} and 10 515 cm^{-1} (1.395 µm and 951 nm, respectively) has been simulated using the most recent (2009) edition of the *HITRAN* database [40]. Definitions of the parameters in the database and their respective units as well as formulae for temperature and pressure corrections to the absorption lines are given in [45].

A human breath sample is assumed to be saturated with water vapour [46]. This means that the breath sample has 100% relative humidity or equivalently that the partial pressure of the water vapour is equal to its saturated vapour pressure at the exhaled temperature. The saturated vapour pressure of a substance is the pressure of the vapour phase when in equilibrium with its non-vapour phases and is dependent on temperature. Assuming atmospheric pressure (1 atm = 101.325 kPa) and 100% humidity inside the lungs, the partial pressure of water vapour at the typical temperature of exhaled human breath (37 °C [46]), is approximately 6280 Pa [47], from which a concentration of water molecules can be estimated through the ideal gas law:

$$\frac{N}{V} = \frac{P}{k_{\mathrm{B}}T} = 1.47 \times 10^{18}\,\mathrm{cm}^{-3}. \tag{5.32}$$

The absorption coefficient, $\alpha(\tilde{\nu})$, of water vapour under these conditions has been calculated in the regions containing the first and second overtones of ethanol's O-H stretch vibration. While similar numbers of water absorption lines are tabulated in these regions, the strongest line in the first overtone region is roughly two orders of magnitude greater than the strongest line in the second overtone region. These transitions are overtones of the symmetric and antisymmetric stretch of the O-H bonds (with fundamental transitions at $3657\,\mathrm{cm}^{-1}$ and $3756\,\mathrm{cm}^{-1}$, respectively [48]). To quantify the integrated absorption intensity of water's O-H stretch overtones compared to that of ethanol, ratios of band intensities of the fundamental to the overtone bands of these transitions were calculated and are shown with those of ethanol from [44] in Fig. 5.12. This enabled determination of how the sensitivity to ethanol concentration would change between overtone regions. The band intensities of overtones of water drop off more quickly than those of ethanol owing to the difference in

the anharmonicity of the O-H stretch vibrations of these two molecules. This means that although the integrated band intensity of ethanol is lower in the second overtone, its relative band intensity is greater than that of water and therefore the composite spectrum is more sensitive to ethanol concentration in the second overtone than the first [48].

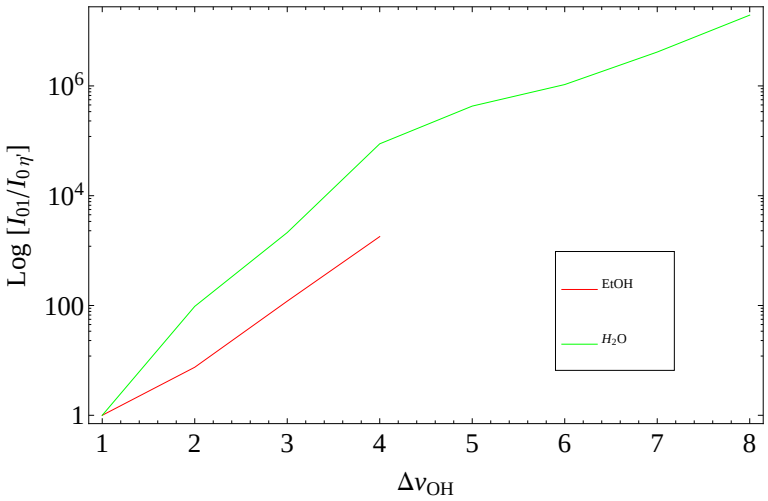

Figure 5.12: Relative O–H vibrational band intensities of EtOH (from [44]) and H_2O (calculated from *HITRAN*). Relative band intensities are obtained by dividing the fundamental band intensity by that of the overtones.

5.3.4 Proposed ethanol detection scheme

An optical approach to detecting concentrations of ethanol in a human breath sample relies on measuring changes in the absorption spectrum of the breath sample. Usually, calculating species concentration from measured absorption peaks directly requires careful calibration of absolute incident and transmitted intensities to detected voltages, and accessible spectral regions free from other absorbing species. Unfortunately, human breath inevitably contains water vapour which absorbs light

throughout much of the same visible and IR regions. Given this, our research group has proposed a detection scheme that relies on the presence of water absorption and is self-calibrating.

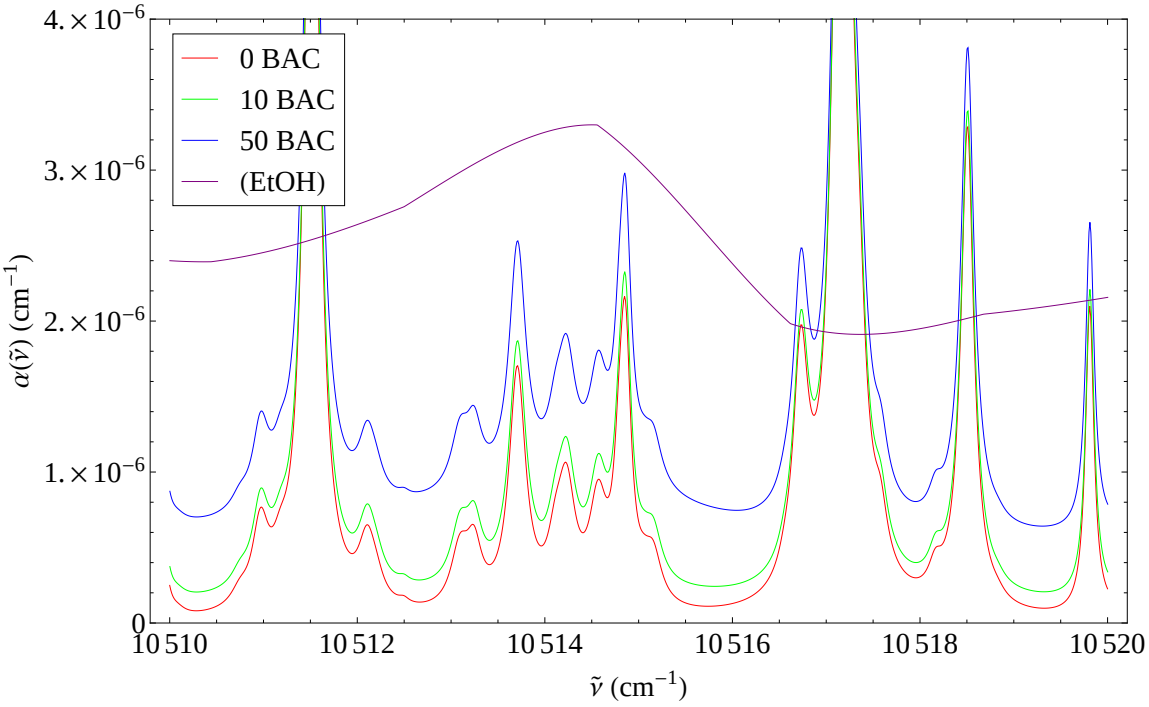

Figure 5.13: Simulated absorption coefficient of EtOH and H_2O vapour at 37 °C, 1 atm, 100% humidity for different concentrations of EtOH using *HITRAN* and experimental data from [43]. The estimated absorption coefficient of EtOH alone is scaled for reference.

Water vapour absorption features are orders of magnitude narrower than even the narrowest of ethanol features (which for the O-H stretch overtones is the Q-branch peak of the *trans*-conformer). The absorption in the vicinity of a water vapour peak that lies within the Q-branch will increase significantly with ethanol concentration compared to an equally strong water peak away from the Q-branch (see Fig. 5.13). Therefore, the relative heights within the spectrum itself can be correlated with a specific concentration of ethanol in the sample if the absorption cross-section of ethanol

Table 5.1: Simulated values for the absorption coefficient of human breath samples at 37 °C, 1 atm and 100% humidity containing different concentrations of ethanol vapour at the positions of water peaks at $10\,516.7\,\mathrm{cm}^{-1}$ and $10\,514.9\,\mathrm{cm}^{-1}$ and ratios between these values. The per-cent change in each ratio compared to the ratio in the absorption coefficient of water vapour alone at these positions is also given.

BAC	$\alpha_1 = \alpha(10\,516.7\,\mathrm{cm}^{-1})$	$\alpha_2 = \alpha(10\,514.9\,\mathrm{cm}^{-1})$	α_1/α_2	% change
0	$1.974\,80 \times 10^{-6}$	$2.163\,38 \times 10^{-6}$	0.912830	0.00
1	$1.984\,99 \times 10^{-6}$	$2.179\,75 \times 10^{-6}$	0.910653	0.24
4	$2.015\,57 \times 10^{-6}$	$2.228\,84 \times 10^{-6}$	0.904312	0.93
10	$2.076\,71 \times 10^{-6}$	$2.327\,02 \times 10^{-6}$	0.892434	2.23
50	$2.484\,37 \times 10^{-6}$	$2.981\,59 \times 10^{-6}$	0.833237	8.72
80	$2.790\,11 \times 10^{-6}$	$3.472\,51 \times 10^{-6}$	0.803486	11.97

at those spectral positions and the absorbing path length are known. Since the measurement is a relative one, *absolute* incident and transmitted light intensities are not necessary for determining concentration and therefore calibration of photodetectors is not required.

As an example, ratios in the simulated absorption coefficient of a human breath sample saturated with water vapour at 37 °C and 1 atm containing different concentrations of ethanol vapour were calculated and are shown in Table 5.1. These ratios were calculated between the positions of comparable water peaks at $10\,514.9\,\mathrm{cm}^{-1}$ and $10\,516.7\,\mathrm{cm}^{-1}$ lying within and away from the Q-branch of *trans*-ethanol's second O-H stretch overtone, respectively.

In practice, however, ratios in the *transmittance* between these spectral positions would be measured. As a second example, ratios in the transmittance for 1 m, 36 m and 76 m absorbing path lengths (available in compact multi-pass cells [49]) were calculated and are shown in Table 5.2. As can be seen in the table, ratios in transmittance are considerably less sensitive to ethanol concentration than the corresponding ratios in the absorption coefficient. This suggests that the absorption

Table 5.2: Ratios in the simulated transmittance spectrum of human breath samples at 37 °C, 1 atm and 100% humidity containing different concentrations of ethanol vapour. Ratios are between positions of water peaks at 10 516.7 cm^{-1} and 10 514.9 cm^{-1} for 1 m, 36 m and 76 m absorption path lengths. The per-cent change in each ratio compared to the ratio in the transmittance of water vapour alone is also given.

BAC	$L = 1$ m	% change	$L = 36$ m	% change	$L = 76$ m	% change
0	0.999981	0.00000	0.999321	0.000	0.998568	0.000
1	0.999981	0.00006	0.999299	0.002	0.998521	0.005
4	0.999979	0.00025	0.999233	0.009	0.998380	0.019
10	0.999975	0.00062	0.999099	0.022	0.998099	0.047
50	0.999950	0.00309	0.998212	0.111	0.996228	0.234
80	0.999932	0.00494	0.997546	0.178	0.994827	0.375

cross-section of ethanol in this region may not be of a sufficient strength for accurate quantitative detection of ethanol concentration using an optical approach. Furthermore, the success of this approach ultimately depends on the sensitivity acheiveable by silicon photodetectors and the effect of increasing path length in multi-pass cells on the signal-to-noise ratio of the detected signal.

5.4 Breathalyser design concept

The main criteria to be fulfilled for a portable optical breathalyser unit are robustness, longevity, inexpensive components and capability to detect ethanol concentrations down to 4 BAC with 1 BAC resolution. A robust design means that the device should have no moving parts since its alignments could easily be affected if the unit is dropped or struck. An angle-resolved etalon configuration would satisfy this criterion since incident light rays with a spread of angles (i.e. θ is the 'scannable' parameter) can be produced with a fixed lens. LED light sources are known to be quite stable and long-lasting and are available in many 'colours' throughout the IR spectrum. Choosing the

region of ethanol's second O-H stretch overtone near $10\,515\,\mathrm{cm}^{-1}$ (951 nm) enables the use of inexpensive silicon photodetectors. Furthermore, a silicon-based CMOS megapixel image sensor is compatible with the angle-resolved etalon configuration. Multi-pass absorption cells offer tens to hundreds of meters of effective absorption path length in a small volume [50], allowing for significant absorption in a portable unit with the aim of providing fine resolution in quantitative ethanol detection.

The optical path of the proposed design would be as follows: a collimated beam of ultra-narrow band light produced by a high-power near-IR LED with a central wavelength of 950 nm and a reflecting Bragg grating band-pass filter with wavenumber bandwidth would enter a multi-pass absorption cell containing the breath sample. Upon exiting the cell, the light would be focused at a position just in front of the etalon by a fixed lens. Upon leaving the etalon, the diverging light rays would be collimated by a second lens such that a full fringe would fill the active area of the CMOS image sensor in a manner according to [38]. The well known positions of water vapour absorption peaks would be used to calibrate the frequency-space Fourier transform of the spatial fringe pattern recorded by the image sensor. Ratios of transmitted intensities between spectral positions most sensitive to ethanol concentration would subsequently be calculated allowing determination of the ethanol concentration following calibration of the multi-pass absorbing path length and precise knowledge of ethanol's absorption cross-section at these positions.

Chapter 6

Conclusion

In this thesis, two applications involving precision measurements of light from semiconductor light sources were investigated. In *Part I*, the rotating quarter-wave plate method, a well-known technique for measuring the polarization state of light, was refined and an InGaAsP laser diode was employed for experimental testing. A polarimeter in which each of the retarder and linear polarizer could be rotated by 180° about a vertical axis allowed the reflection of the optic axes in the horizonatal reference axis. Using linearly polarized incident light, a set of transmitted intensities was recorded for each of the four orientations (called cases herein) of the optics due to this rotation, from which Stokes vectors were calculated for a range of polarimeter parameters, β_0, Δ and γ. An additional parameter, ϕ, was included to account for the possible misalignment of the vertical rotation axes of the two optics. The set of parameters that generated the minimum least squares error between the derived Stokes vectors for the four cases and a derived degree of polarization consistent with that of fully-polarized incident light best characterized the polarimeter. This was confirmed

by reporting Stokes vectors consistent with that of horizontal linearly polarized incident light obtained from additional test data sets following nine calibrations using three different retardances and three different intentional misalignments.

In *Part II*, a theoretical investigation of the Fabry-Perot interferometer and its application to quantitative absorption spectroscopy was conducted. The transmission functions of ideal and non-ideal etalons with non-monochromatic incident light were modelled to study the effects of possible surface imperfections and finite linewidth sources of different lineshapes on the visibility of interference fringes. Source profiles with steeper fall-off at the edges, such as a top hat profile, were found to have near unity visibility for widths less than the free spectral range due to less leakage of light intensity into adjacent orders. The resolution of an absorption feature within the source profile was then confirmed to be independent of the source width although its visibility decreased as the source width approached and exceeded the free spectral range. Etalon surface imperfections were found to decrease both the resolution and visibility of absorption features. These results were discussed in the context of a possible detection scenario involving samples of ethanol and water vapours. The second overtone of ethanol's O-H stretch vibration was studied due to its accessibility to silicon-based detectors. The water vapour spectrum in this region was simulated from *HITRAN* and a possible ethanol detection scheme involving changes in relative absorption in the vicinity of water lines with ethanol concentration was considered. This investigation has provided the basis for possible further research into the implementation of such a scheme within a portable device employing an LED light source due to the benefit it would bring for this application.

Bibliography

[1] N. Zheludev, "The life and times of the LED – a 100-year history," *Nature Photonics* **1**, 189–192 (2007).

[2] F. G. Smith, T. A. King and D. Wilkins, "LEDs and Semiconductor Lasers," in *Optics and Photonics. An Introduction, Second Edition* (Wiley, 2007), pp. 401–406.

[3] H. G. Berry, G. Gabrielse and A. E. Livingston, "Measurement of the Stokes parameters of light," *Appl. Opt.* **16**, 3200–3205 (1977).

[4] C. Flueraru, S. Latoui, J. Besse and P. Legendre, "Error analysis of a rotating quarter-wave plate Stokes' polarimeter," *IEEE Trans. Instr. Meas.* **57**, 731–735 (2008).

[5] Comar Optics Inc., http://www.comaroptics.com/

[6] J. S. Tyo and H. Wei, "Optimizing imaging polarimeters constructed with imperfect optics," *Appl. Opt.* **45**, 5497–5503 (2006).

[7] V. A. Dlugunovich, V. N. Snopko and O. V. Tsaryuk, "Analysis of a method for measuring polarization characteristics with a Stokes polarimeter having a rotating phase plate," *J. Opt. Technol.* **68**, 269–273 (2000).

[8] R. L. Brooks and E. H. Pinnington, "Polarization measurements of HeI singlet transitions following beam–tilted-foil excitation," *Phys. Rev. A* **18**, 1454–1458 (1978).

[9] R. L. Brooks, "Polarization studies using beam foil spectroscopy," Ph. D. thesis, U. of Alberta (1979).

[10] E. Hecht, "A mathematical description of polarization," in *Optics Fourth Edition*, A. Black, ed. (Addison Wesley, 2002), pp. 373–379.

[11] E. Compain, S. Poirier and B. Drevillon, "General and self-consistent method for the calibration of polarization modulators, polarimeters, and Mueller-matrix ellipsometers," *Appl. Opt.* **38**, 3490–3502 (1999).

[12] B. Schaefer, E. Collett, R. Smyth, D. Barrett and B. Fraher, "Measuring the Stokes polarization parameters," *Am. J. Phys.* **75**, 163–168 (2006).

[13] P. A. Williams, "Rotating-wave-plate Stokes polarimeter for differential group delay measurements of polarization-mode dispersion," *Appl. Opt.* **38**, 6508–6515 (1999).

[14] M. Born and E. Wolf, *Principles of Optics* (CUP, 1999).

[15] F. L. Pedrotti, S. J. Pedrotti and L. M. Pedrotti, "Spot Size and Radius of Curvature of a Gaussian Beam," in *Introduction to Optics Third Edition* (Pearson Prentice Hall, 2007), pp. 586–590.

[16] A. E. Siegman, "How to (maybe) measure laser beam quality," Tutorial presentation at the OSA annual meeting, Long Beach, California (Oct. 1997).

[17] A. E. Siegman, "Defining, measuring, and optimizing laser beam quality," *SPIE* **1868**, 2-12 (1993).

[18] Microchip Technology Inc., http://www.microchip.com/

[19] M. Fox, *Optical Properties of Solids* (OUP, 2010).

[20] M. Bass, *Handbook of Optics* (McGraw–Hill, 2000).

[21] M. S. El-Bahrawi, N. N. Nagib, S. A. Khodier and H. M. Sidki, "Birefringence of muskovite mica," *Opt. Laser Technol.* **30** 411–415 (1998).

[22] C. Fabry and A. Perot, "Sur les franges des lames minces argentées et leur application a la mesure de petites épasseurs d'air." *Ann. Chim. Phys.* **12**, 459–501 (1897).

[23] K. Burns and W. F. Meggers, *Pub. Allegheny Obs.* **6**, 105 (1927).

[24] K. W. Meissner, "Interference spectroscopy. Part II," *J. Opt. Soc. Amer.* **32**, 185–210 (1942).

[25] P. J. Treanor, "A new heterochromatic Fabry-Perot fringe system applicable to the inferometry of absorption spectra," *Nature* **162**, 885–886 (1948).

[26] J. H. Jaffe, "An interference spectrometer for the infra-red," *Nature* **168**, 381–382 (1951).

[27] J. H. Jaffe, T. A. Wiggins and D. H. Rank, "Extreme resolution of infra-red absorption spectra," *Nature* **175**, 908 (1955).

[28] J. H. Jaffe, D. H. Rank and T. A. Wiggins, "High resolution in the infrared by interferometry. Unambiguous display without overlapping orders," *J. Opt. Soc. Amer.* **45**, 636–643 (1955).

[29] A. Walsh, "Design of multiple-monochromators," *Nature* **167**, 810–811 (1951).

[30] D. H. Rank, E. R. Shull and T. A. Wiggins, "High resolution spectroscopy of the infrared," *J. Opt. Soc. Amer.* **43**, 214–215 (1953).

[31] W. Kaye, "Near-infrared spectroscopy II. Instrumentation and technique," *Spectrochimica Acta* **7**, 181–204 (1955).

[32] P. Jacquinot, "The luminosity of spectrometers with prisms, gratings, or Fabry-Perot etalons," *J. Opt. Soc. Amer.* **44**, 761–765 (1954).

[33] J. M. Hollas, "General features of experimentation," in *High Resolution Spectroscopy, Second Edition* (Wiley, 1998), pp. 47–48.

[34] F. L. Pedrotti, S. J. Pedrotti and L. M. Pedrotti, "Fabry-Perot Transmission: The Airy Function," in *Introduction to Optics Third Edition* (Pearson Prentice Hall, 2007), pp. 201–206.

[35] G. Hernandez, "Real sources," in *Fabry-Perot Interferometers*, P. L. Knight, W. J. Firth and S. D. Smith, FRS, eds. (Cambridge University Press, 1986), pp. 20–23.

[36] M. L. Boas, *Mathematical Methods in the Physical Sciences Second Edition* (Wiley, 1983), pp. 568–569.

[37] R. Chabbal, "Recherche des meuilleures conditions d'utilisation d'un spectromètre photoélectrique Fabry-Perot," *J. Rech. Centre Natl. Rech. Sci. Lab. Bellevue* (Paris) **5**, 138–186 (1953).

[38] J. N. Philippson, M. Ugray, T. J. Toai and R. C. Shiell, "Compact angle-resolved optical spectrum analyzer using a programmable microcontroller approach," *J. Opt. A: Pure Appl. Opt.* **9**, 1024–1029 (2007).

[39] http://www.optigrate.com/BragGrate_Bandpass.html

[40] http://www.cfa.harvard.edu/hitran/

[41] D. J. Donaldson, G. J. Frost, K. H. Rosenlof, A. F. Tuck and V. Vaida, "Atmospheric radical production by excitation of vibrational overtones via absorption of visible light," *Geophys. Res. Lett.* **24**, 2651–2654 (1997).

[42] K. Takahashi, M. Sugawara and S. Yabushita, "Theoretical analysis on the fundamental and overtone OH stretching spectra of several simple acids and alcohols," *J. Phys. Chem. A* **107**, 11092–11101 (2003).

[43] H. L. Fang and R.L. Swofford, "Molecular conformers in gas-phase ethanol: a temperature study of vibrational overtones," *Chem. Phys. Lett.* **105**, 5–11 (1984).

[44] K. R. Lange, N. P. Wells, K. S. Plegge and J. A. Phillips, "Integrated intensities of O-H stretching bands: fundamentals and overtones in vapor-phase alcohols and acids," *J. Phys. Chem. A* **2001**, 3481–3486 (2001).

[45] L. S. Rothman *et al.* "The *HITRAN* 2004 molecular spectroscopic database," *JQSRT* **96**, 139–204 (2005).

[46] P. Španěl, D. Smith, "On-line measurement of the absolute humidity of air, breath and liquid headspace samples by selected ion flow tube mass spectrometry." *Rapid Commun. Mass Spectrom.* **15**, 563–569 (2001).

[47] "Vapour Pressure of Water Below 100°," in *CRC Handbook of Chemistry and Physics, 55th Edition*, R. C. Weast, ed. (CRC Press, 1974), p. D159.

[48] P. F. Bernath, "Vibrational Selection Rules for Diatomics," in *Spectra of Atoms and Molecules, Second Edition* (Oxford, 2005), pp. 216–220.

[49] http://www.aerodyne.com/products/astigmatic-multipass-absorption-cells

[50] J. B. McManus, P. L. Kebabian, and M. S. Zahniser, "Astigmatic mirror multipass absorption cells for long-path-length spectroscopy," *Appl. Opt.* **34**, 3336–3348 (1995).

[51] H. B. Dwight, *Tables of Integrals and Other Mathematical Data Fourth Edition* (Macmillan, 1961), p. 91.

[52] H. B. Dwight, *Tables of Integrals and Other Mathematical Data Fourth Edition* (Macmillan, 1961), p. 236.

[53] H. B. Dwight, *Tables of Integrals and Other Mathematical Data Fourth Edition* (Macmillan, 1961), p. 224.

Appendix A

Convolution integrals

Gaussian

$$
\begin{aligned}
Y_G(\delta) &= S_G * Y \\
&= \int_{-\infty}^{\infty} S_G(y) Y(\delta - y) dy \\
&= \frac{(1-R)^2}{\sqrt{\pi} G} \int_{-\infty}^{\infty} \frac{e^{-y^2/G^2} dy}{1 - 2R\cos(\delta - y) + R^2} \\
&= \frac{1-R}{1+R} \frac{1}{\sqrt{\pi} G} \int_{-\infty}^{\infty} e^{-y^2/G^2} \left[1 + 2 \sum_{k=1}^{\infty} R^k \cos k(\delta - y) \right] dy \\
&= \frac{1-R}{1+R} \frac{1}{\sqrt{\pi} G} \int_{-\infty}^{\infty} e^{-y^2/G^2} \left[1 + 2 \sum_{k=1}^{\infty} R^k \cos k\delta \cos ky + 2 \sum_{k=1}^{\infty} R^k \sin k\delta \sin ky \right] dy \\
&= \frac{1-R}{1+R} \left[1 + \frac{2}{\sqrt{\pi} G} \sum_{k=1}^{\infty} R^k \left(\int_{-\infty}^{\infty} e^{-y^2/G^2} \cos ky dy \right) \cos k\delta \right] \\
&= \frac{1-R}{1+R} \left[1 + 2 \sum_{k=1}^{\infty} R^k e^{-k^2 G^2/4} \cos k\delta \right],
\end{aligned}
\tag{A.1}
$$

where [51, 52]:

$$\frac{1-R^2}{1-2R\cos y+R^2} = 1+2\sum_{k=1}^{\infty} R^k \cos ky, \quad R^2<1, \tag{A.2}$$

$$\int_0^{\infty} e^{-y^2/G^2}\cos ky\, dy = \frac{\sqrt{\pi}G}{2}\, e^{-k^2G^2/4}, \quad G>0. \tag{A.3}$$

Lorentzian

$$\begin{aligned}
Y_L(\delta) &= S_L * Y \\
&= \int_{-\infty}^{\infty} S_L(y)Y(\delta-y)dy \\
&= \frac{(1-R)^2L}{\pi}\int_{-\infty}^{\infty}\frac{dy}{(L^2+y^2)[1-2R\cos(\delta-y)+R^2]} \\
&= \frac{(1-R)L}{(1+R)\pi}\int_{-\infty}^{\infty}\frac{\left[1+2\sum_{k=1}^{\infty}R^k\cos k(\delta-y)\right]}{L^2+y^2}\,dy \\
&= \frac{(1-R)L}{(1+R)\pi}\int_{-\infty}^{\infty}\frac{\left[1+2\sum_{k=1}^{\infty}R^k\cos k\delta\cos ky+2\sum_{k=1}^{\infty}R^k\sin k\delta\sin ky\right]}{L^2+y^2}dy \\
&= \frac{1-R}{1+R}\left[1+\frac{2L}{\pi}\sum_{k=1}^{\infty}R^k\left(\int_{-\infty}^{\infty}\frac{\cos ky}{L^2+y^2}dy\right)\cos k\delta\right] \\
&= \frac{1-R}{1+R}\left[1+2\sum_{k=1}^{\infty}(Re^{-L})^k\cos k\delta\right],
\end{aligned} \tag{A.4}$$

where [53]:

$$\int_0^{\infty}\frac{\cos ky}{L^2+y^2}\,dy = \frac{\pi}{2L}\,e^{-kL}, \quad L>0;\ k\geq 0. \tag{A.5}$$

Top hat

$$
\begin{aligned}
Y_{\Pi}(\delta) &= S_{\Pi} * Y \\
&= \int_{-\infty}^{\infty} S_{\Pi}(y) Y(\delta - y) dy \\
&= \frac{(1-R)^2}{W} \int_{-W/2}^{W/2} \frac{dy}{1 - 2R\cos(\delta - y) + R^2} \\
&= \frac{1-R}{(1+R)W} \int_{-W/2}^{W/2} \left[1 + 2\sum_{k=1}^{\infty} R^k \cos k(\delta - y) \right] dy \\
&= \frac{1-R}{(1+R)W} \int_{-W/2}^{W/2} \left[1 + 2\sum_{k=1}^{\infty} R^k \cos k\delta \cos ky + 2\sum_{k=1}^{\infty} R^k \sin k\delta \sin ky \right] dy \\
&= \frac{1-R}{1+R} \left[1 + \frac{2}{W} \sum_{k=1}^{\infty} R^k \left(\int_{-W/2}^{W/2} \cos ky dy \right) \cos k\delta \right] \\
&= \frac{1-R}{1+R} \left[1 + 2\sum_{k=1}^{\infty} R^k \frac{2}{kW} \sin(kW/2) \cos k\delta \right] \\
&= \frac{1-R}{1+R} \left[1 + 2\sum_{k=1}^{\infty} R^k \mathrm{sinc}(kW/2) \cos k\delta \right].
\end{aligned}
\tag{A.6}
$$